

Neutrino Signals of Core-Collapse Supernovae in Underground Detectors

Shaquann Seadrow,^{1*} Adam Burrows,¹ David Vartanyan,¹ David Radice^{1,2}
and M. Aaron Skinner³

¹*Department of Astrophysical Sciences, Princeton University, Princeton, NJ 08544*

²*Schmidt Fellow, Institute for Advanced Study, 1 Einstein Drive, Princeton, NJ 08540*

³*Livermore National Laboratory, 7000 East Ave., Livermore, CA 94550-9234*

Accepted XXX. Received YYY; in original form ZZZ

ABSTRACT

For a suite of fourteen core-collapse models during the dynamical first second after bounce, we calculate the detailed neutrino “light” curves expected in the underground neutrino observatories Super-Kamiokande, DUNE, JUNO, and IceCube. These results are given as a function of neutrino-oscillation modality (normal or inverted hierarchy) and progenitor mass (specifically, post-bounce accretion history), and illuminate the differences between the light curves for 1D (spherical) models that don’t explode with the corresponding 2D (axisymmetric) models that do. We are able to identify clear signatures of explosion (or non-explosion), the post-bounce accretion phase, and the accretion of the silicon/oxygen interface. In addition, we are able to estimate the supernova detection ranges for various physical diagnostics and the distances out to which various temporal features embedded in the light curves might be discerned. We find that the progenitor mass density profile and supernova dynamics during the dynamical explosion stage should be identifiable for a supernova throughout most of the galaxy in all the facilities studied and that detection by any one of them, but in particular more than one in concert, will speak volumes about the internal dynamics of supernovae.

Key words: neutrinos – (stars:) supernovae: general – stars: interiors

1 INTRODUCTION

Neutrinos are produced and radiated at very high rates during and immediately after the collapse of the core of a massive star ($M \geq 8 M_{\odot}$) at its terminal stages (Burrows, Klein, & Gandhi 1992; Fischer et al. 2009; Müller & Janka 2014; Nakamura et al. 2016). For seconds during its dynamical and supernova phases, the core transitions into a proto-neutron star (PNS; Burrows & Lattimer 1986), its neutrino emissions directly reflecting in real time the internal dynamics of this violent phenomenon. Theory identifies neutrinos as the drivers of explosion (Bethe & Wilson 1985) and of the evolution of the nascent PNS. As such, neutrinos are the primary diagnostics of all stages of core behavior after stellar death and before the emergence of the residual neutron star or black hole. Stamped on the associated neutrino light curves, spectra, and mix of emitted neutrino species as a function of time are the distinctive signatures of the collapse, bounce, shock breakout, accretion, explosion, and PNS cool-

ing phases, otherwise obscured from direct scrutiny by the profound opacity to photons of the overlying stellar matter (Burrows 1990; Burrows, Hayes, & Fryxell 1995; Fischer et al. 2009; Müller & Janka 2014; Mirizzi et al. 2016; Nakamura et al. 2016; Horiuchi & Kneller 2017). By the high signal rate, followed by a abrupt cessation, one can witness in the neutrino emission history the formation, if it occurs, of a black hole (Burrows 1984,1988; Sumiyoshi et al. 2006; Fischer et al. 2009). The shock breakout burst in electron neutrinos is a firm prediction of theory that must be tested (Thompson, Burrows, & Pinto 2003; Wallace, Burrows, & Dolence 2016). The rapid neutrino light-curve variations due to turbulence in the core can constrain the convective physics predicted in most multi-dimensional models (Lund et al. 2010,2012; Tamborra et al. 2013) and considered essential to the generic mechanism of explosion (Herant et al. 1992; Burrows, Hayes, & Fryxell 1995; Janka & Müller 1996).

The supernova neutrino burst has been detected only once, from the supernova SN1987A at ~ 50 kiloparsecs (kpc) in the large Magellanic Cloud (Hirata et al. 1987; Bionta

* E-mail: shaquannseadrow@gmail.com

et al 1987). However, a total of only 11 and 8 events over ~ 12.5 and ~ 5.5 seconds, respectively, were culled. While the crude basics of PNS formation and cooling were verified in broad outline (Burrows & Lattimer 1986, 1987), the signal rates in these relatively small detectors at this extragalactic distance were paltry and most of the predicted phenomena were grossly undersampled. However, with the advent of numerous large-volume/mass underground detectors for the measurement of solar and atmospheric neutrinos (Super-Kamiokande, Abe et al. 2016; IceCube, Abbasi et al. 2011, Köpke et al. 2011) and neutrino oscillation parameters (DUNE, Ankowski et al. 2016; JUNO, Lu et al. 2015), a network of highly-capable facilities is being assembled that could record many thousands of neutrino events from a galactic core-collapse supernova (CCSN) explosion (Scholberg 2012; Beck et al. 2013). Super-K (~ 32.5 kilotonnes detecting volume) may be followed by Hyper-K (Abe et al. 2011, 2018; ~ 0.25 – 0.4 Megatonnes) may be able to reach out to the Andromeda galaxy (M31) at ~ 700 kiloparsecs (kpc). With such detectors, the detailed evolution of 1) the neutrino spectra of the various neutrino types (Gallo Rosso et al. 2018), 2) the breakout burst, 3) the variation in the mass accretion rate post-bounce, but prior to explosion, 4) the accretion of shell interfaces (such as that at the boundary of the silicon and oxygen shells), 5) the explosion itself, and 6) the temporal fluctuations due to turbulent convection behind the shock could all be captured, identified, and studied.

Hence, detecting such a high-signal galactic burst and its detailed scrutiny are essential to validate and fundamentally constrain the theory of CCSN that has emerged over the last fifty years. The theory of the CCSN explosion and the theory of massive star evolution to Chandrasekhar collapse (Woosley & Weaver 1995; Woosley, Heger, & Weaver 2002; Hirschi, Meynet, & Maeder 2004; Woosley & Heger 2007; Maeder & Meynet 2012; Sukhbold et al. 2016) are intimately intertwined, so the latter is tested as well if a high-event rate galactic supernova is witnessed.

In this paper, we do not explore all the various neutrino signatures of the multi-second evolution of the supernova core, nor the retrieval in detail of the multiple parameters and inputs to CCSN theory. This would be too large a task, though aspects of this will be relegated to future installments in our series on core-collapse signatures and diagnostics¹. Rather, using recently generated two-dimensional (2D) and one-dimensional (1D) multi-group radiation/hydrodynamic models employing the code FORNAX (Burrows et al. 2018; Radice et al. 2017, Skinner et al. 2016; Wallace et al. 2016; Vartanyan et al. 2018; Skinner et al. 2018), we focus on the general overarching features of the neutrino light curve in Super-K, DUNE, JUNO, and IceCube during approximately the first second after bounce as a function of progenitor mass and between exploding and non-exploding models. The first second is the most dynamical phase. We also explore the potential identification of features in the accreted density structure, such as the silicon/oxygen interface, and estimate the effects of neutrino oscillations on

the detected signals (Mirizzi et al. 2016; Scholberg 2018). We use the 9, 10, 11, 16, 17, 19, and 21 M_{\odot} progenitor models of Sukhbold et al. (2016), as evolved in Radice et al. (2017), Burrows et al. (2018), and Vartanyan et al. (2018), for our representative progenitor model suite. The 2D variants of these models explode (Vartanyan et al. 2018; Burrows et al. 2018; Radice et al. 2017), while the spherically-symmetric 1D models do not. We use this difference to gauge the difference between exploding and non-exploding models and find that after explosion the neutrino event rate is diagnostically very different between them. Also, we can identify in many of the non-exploding models a clear signature of the accretion of the silicon/oxygen interface. Moreover, we see other characteristic timescales that can readily be discerned, as well as clear differences in all detectors between event-rate models in the various detectors for non-oscillation, normal-hierarchy, and inverted-hierarchy realizations.

We emphasize that the differences between the 1D and 2D models and between non-exploding and exploding models are not strictly related to the specifics of our hydrodynamic models, but to the signature in underground detectors of the cessation of accretion power due to explosion. This is a generic prediction of supernova theory and is not specific to our models. In theory, the neutrino emissions from a supernova (or the collapsed core of a massive star) are powered by two sources - diffusion from the core and accretion onto the core. Given an initial density profile, reflected in the initial progenitor model, the neutrino emissions after bounce and before explosion are determined by this initial structure (given the physics of transport, equation of state, etc.). Hence, there is a direct mapping between the progenitor structure (represented in the literature and in this paper by the progenitor mass) and the pre-explosion neutrino emissions. The onset of explosion inaugurates the cessation (and reversal) of accretion, withdrawing this component from powering the emergent neutrino luminosity. 1D, 2D, and 3D models of this emission before explosion are very closely the same, since the inner core from which the neutrinos emerge is always pseudo-spherical. This is seen before explosion in the luminosity and signal plots provided in §6. The multi-D effects are predominantly turbulence behind the shock, shown in the literature to be crucial to explosion, but still roughly averaging to spherical accretion (with some rapid temporal fluctuations), as far as the emergent neutrino emissions are concerned. Turbulence introduces, among other things, a turbulent pressure that aids and enhances “explodability” and brings the core to the critical condition for explosion.

We reiterate that even if core collapse does not result in a supernova explosion, the neutrino signal from such a core will be robust and observable. For our galaxy, non-exploding models have signal rates and total event counts that are comparable to (and at later post-bounce times generally even larger than) those for exploding models. The neutrino facilities will easily see this (if they are online), even if there is no optical counterpart. It is the differences between exploding models and non-exploding models (represented in this paper by 2D versus 1D models), due to the cessation of accretion in the former, that we contend can be distinguished when the next core collapse occurs in our galactic neighborhood.

Our purpose with this paper is not to rehash this theory, but to demonstrate differences, in principle detectable

¹ Currently, in this series are Wallace et al. (2016) on the neutrino breakout burst and Morozova et al. (2018) on the gravitational wave emissions and characteristics.

in underground neutrino facilities, between exploding and non-exploding models that are generic predictions of general core-collapse supernova theory. The prediction that there is a transition at explosion from accretion plus core diffusion in the sourcing of the neutrino emissions to solely diffusion, and the concomitant decrease at explosion and afterward of the neutrino signal(s), is an experimentally testable hypothesis of current theory. In this paper, we provide not just one model for signals, but a full suite, to quantify the expected approximate trends from low to higher mass supernova progenitors. Most papers exploring signals provide only one or two models, so doing the multitude of models we have presented here is new to this paper.

In section 2, we summarize our method of calculating a neutrino light curve in the typical detector. We include in §3 a short discussion on incorporating adiabatic neutrino oscillations. We follow this in section 4 with descriptions of the various underground neutrino detectors highlighted in this paper. Then, in section 5, we summarized the salient features of FORNAX and of the 2D and 1D multi-group radiation/hydro models generated using it, and follow in section 6 with our results for the various neutrino light curves in Super-K, DUNE, JUNO, and IceCube. Sections 6.2 and 6.3 contains a general discussion of the implications of our results and section 7 summarizes our conclusions. We postpone to another paper the investigation of the extraction of the neutrino energy spectrum and of the species mix of the neutrinos emitted.

2 SIGNAL CALCULATION METHOD

In this paper, we explore the characteristic neutrino signatures in various representative underground neutrino detectors during the first crucial and dynamical second after core bounce of the supernova phenomenon. We investigate their dependence upon progenitor mass, distance, oscillation modality, and detector capabilities. The core-collapse models (§5) were generated by our FORNAX code (Skinner et al. 2016; Radice et al. 2017; Burrows et al. 2018; Vartanyan et al. 2018) and we employ the SNOwGLOBES software package (Hubber et al. 2010; Beck et al. 2013; Scholberg 2018) for computing the detected event rates in the chosen constellation of underground detectors. We have produced a pipeline that allows us easily to change the neutrino source, distance, and detector.

The neutrino energy spectra are calculated at 10,000 km from the center of each progenitor for models using either the LS220 EOS (equation of state) or the SFHO EOS. Since our focus is on the general signal characteristics of exploding vis à vis non-exploding models (§5), where all the 2D (axisymmetric) models we show explode and all the corresponding 1D (spherical) models do not, the specific EOS employed for each model is of secondary concern. We lump together the ν_μ , $\bar{\nu}_\mu$, ν_τ , and $\bar{\nu}_\tau$ neutrinos into “ ν_x ” a neutrino bin, and distinguish the electron-type (ν_e) and anti-electron-type ($\bar{\nu}_e$) species. All three species have distinct spectra and temporal evolutions. SNOwGLOBES accounts for the multitude of interactions and channels in each detector caused by each species. In an intermediate step required for signal determination, we convert the energy spectra, $\frac{dL_\nu(E_\nu, t)}{dE_\nu}$, into

number-luminosity spectra:

$$\frac{d^2 N_\nu}{dE_\nu dt} = \frac{dL_\nu(E_\nu, t)}{dE_\nu} \frac{1}{E_\nu}. \quad (1)$$

For a given detector, the event rate for any given channel is

$$\frac{dN_{det}}{dt} = N_{tar} \frac{1}{4\pi D^2} \int \frac{d^2 N_\nu}{dE_\nu dt} \sigma(E_\nu) \epsilon(E) dE_\nu, \quad (2)$$

where N is the number of detected events, N_ν is (as above) the number of emitted neutrinos, the distance to the supernova is D , the number of target atoms in a given detector is N_{tar} , and the neutrino-energy-dependent cross section for a given interaction channel is $\sigma(E_\nu)$. The efficacy of neutrino detection also depends upon the efficiency of the detectors, $\epsilon(E)$, where E is the energy of the final-state product (such as an electron). This is approximately 1.0 above some detector-dependent threshold and 0.0 below it. In water Cherenkov detectors such as Super-K this threshold is ~ 5 MeV. Given the detectors we have chosen to highlight, we focus on neutrino interactions in water, ice, scintillator, and liquid argon. SNOwGLOBES imposes a particular energy binning. As a result, our model spectra, which are grouped into 20 logarithmically-spaced energy bins from 1 MeV to either 300 (for ν_{es}) or 100 MeV (for $\bar{\nu}_{es}$ and ν_{s}) (Radice et al. 2017), must be mapped onto its grid. We do this using a straightforward interpolant, which executes one-dimensional monotonic cubic splines, across SNOwGLOBES’s energy range from 0.5 to 100 MeV.

When estimating the statistical errors in the time bins selected when binning the signals (and these bin widths can be arbitrary), we multiply the height (signal rate) by the bin width, Δt , take the square root, and then divide by the bin width. Thus, we calculate the event rate error (σ) for each bin using the simple formula:

$$\sigma \Delta t = \sqrt{\frac{dN_{det}}{dt}} \Delta t. \quad (3)$$

In this way, we obtain a measure of the error in the signal rate for the given bin width. This, of course, is a function of distance. If we choose a wide bin width, the error in the average signal rate around that time bin is perforce lower, but the temporal resolution would be correspondingly diminished. As long as the detectors have good time tagging, this procedure is, of course, arbitrary and to taste. We explore some of the general conclusions using this approach in §6.3.

3 NEUTRINO OSCILLATIONS

The incoming neutrinos, by their nature, undergo neutrino oscillations. To incorporate such oscillations, we employ the approximate approach of Dighe & Smirnov (2000) to account for the adiabatic Mikheyev-Smirnov-Wolfenstein effect in the stellar envelope. This approach for handling neutrino oscillation effects in the context of supernova neutrino detection is similar to, or more sophisticated than, for example that found in Nakamura et al. (2016), Nikrant et al. (2018), Kawogoe et al. (2010), Scholberg (2018), Tambora et al. (2014), Abe et al. (2016), Serpico et al. (2012), Müller & Janka (2014), and Gallo Rosso et al. (2018).

Our only major assumption is adiabaticity, and we ignore for the purposes of clarity additional matter oscillation effects in the Earth. Since the direction from which a neutrino burst would come will be from any angle in an Earth-centered coordinate system, the Earth effects are unpredictable. The associated Earth column traversed by the neutrinos is a priori unknown. Addressing this a priori, therefore, would add an extra degree of complexity generally ignored in the literature. However, slight flavor regeneration while traversing the Earth has less of an effect on the total signal rate upon which we focus in this paper than upon the detailed measured spectra. With a high neutrino energy resolution (perhaps beyond the capability of the current Super-K, but within that anticipated for JUNO), this effect might be discerned and diagnostic. The reader is referred to Liao (2016) for a discussion of this issue. The only non-adiabatic effect of interest may be the encountering by the emergent neutrinos of any steep density jumps in the outer star, perhaps associated with the supernova shock itself (Mirizzi et al. 2016). However, addressing this possibility would introduce, we feel, unnecessary and very uncertain complications associated with special details of the phenomenon and variable outer progenitor structures and is beyond the scope of our thesis. Note that neutrino-neutrino self-refraction effects (Pantaleone 1992; Duan, Fuller, & Qian 2006) do not obtain for these models, due to the dominance of electron lepton number over the neutrino lepton number (Dasgupta, O’Connor, & Ott 2012; Sarikas et al. 2012). It is only for very low-mass massive stars (such as the Nomoto and Hashimoto (1984) 8.8 M_{\odot} model) that self-refraction effects might be of interest, but these models are not in our set.

The resulting mappings are:

$$F_{\nu_e} = pF_{\nu_e}^0 + (1-p)F_{\nu_x}^0, \quad F_{\bar{\nu}_e} = \bar{p}F_{\bar{\nu}_e}^0 + (1-\bar{p})F_{\nu_x}^0,$$

and

$$4F_{\nu_x} = (1-p)F_{\nu_e}^0 + (1-\bar{p})F_{\bar{\nu}_e}^0 + (2+p+\bar{p})F_{\nu_x}^0. \quad (4)$$

In these equations, the initial flux of a neutrino species is F_i^0 and the survival probabilities are p and \bar{p} . Dighe & Smirnov (2000) also assume that the total flux of the heavy lepton species satisfies:

$$4F_{\nu_x} = F_{\nu_{\mu}} + F_{\nu_{\tau}} + F_{\bar{\nu}_{\mu}} + F_{\bar{\nu}_{\tau}}. \quad (5)$$

Utilizing the survival probabilities of Kato et al. (2017) that incorporate the θ_{13} mixing angle, we have for the Normal Hierarchy (NH):

$$p = \sin^2 \theta_{13} \quad \text{and} \quad \bar{p} = \cos^2 \theta_{12} \cos^2 \theta_{13}$$

and for the Inverted Hierarchy (IH):

$$p = \sin^2 \theta_{12} \cos^2 \theta_{13} \quad \text{and} \quad \bar{p} = \sin^2 \theta_{13}.$$

Using these survival probabilities, we, thus, obtain for the Normal Hierarchy:

$$F_{\nu_e} = \sin^2 \theta_{13} F_{\nu_e}^0 + (1 - \sin^2 \theta_{13}) F_{\nu_x}^0, \quad (6)$$

$$F_{\bar{\nu}_e} = \cos^2 \theta_{12} \cos^2 \theta_{13} F_{\bar{\nu}_e}^0 + (1 - \cos^2 \theta_{12} \cos^2 \theta_{13}) F_{\nu_x}^0, \quad (7)$$

and

$$4F_{\nu_x} = (1 - \sin^2 \theta_{13}) F_{\nu_e}^0 + (1 - \cos^2 \theta_{12} \cos^2 \theta_{13}) F_{\bar{\nu}_e}^0 + (2 + \sin^2 \theta_{13} + \cos^2 \theta_{12} \cos^2 \theta_{13}) F_{\nu_x}^0 \quad (8)$$

and for the Inverted Hierarchy:

$$F_{\nu_e} = \sin^2 \theta_{12} \cos^2 \theta_{13} F_{\nu_e}^0 + (1 - \sin^2 \theta_{12} \cos^2 \theta_{13}) F_{\nu_x}^0, \quad (9)$$

$$F_{\bar{\nu}_e} = \sin^2 \theta_{13} F_{\bar{\nu}_e}^0 + (1 - \sin^2 \theta_{13}) F_{\nu_x}^0, \quad (10)$$

and

$$4F_{\nu_x} = (1 - \sin^2 \theta_{12} \cos^2 \theta_{13}) F_{\nu_e}^0 + (1 - \sin^2 \theta_{13}) F_{\bar{\nu}_e}^0 + (2 + \sin^2 \theta_{12} \cos^2 \theta_{13} + \sin^2 \theta_{13}) F_{\nu_x}^0 \quad (11)$$

When accounting for oscillations, we use the best fit mass-mixing parameters from Capozzi et al. (2017): $\sin^2(\theta_{12}) = 2.97 \times 10^{-1}$ and $\sin^2(\theta_{13}) = 2.15 \times 10^{-2}$ for both hierarchies. The high electron densities around the inner core for these models allows us to ignore self-refraction effects on the emergent neutrino spectra, and, as implied, we ignore any possible non-adiabatic oscillation effects due to shocks and at steep compositional interfaces.

We see from equations (6) through (10) and the values of the oscillation angles that for the normal hierarchy ν_e s in a detector come mostly from ν_x s at the source and $\bar{\nu}_e$ s at the detector are a mix of ν_x s and $\bar{\nu}_e$ s at the source. For the inverted hierarchy, to a slightly greater degree than for the normal hierarchy ν_x s source ν_e s at the detector, while $\bar{\nu}_e$ s in a detector were once ν_x s (even more so than for the normal hierarchy). These mappings are relevant for the differences in the event rates for the various detectors (differentially sensitive as they are to the various neutrino flavors) and hierarchies.

4 UNDERGROUND DETECTOR CHARACTERISTICS

4.1 Super-Kamiokande

Super-Kamiokande (Super-K; SK) is a ~ 50 -ktonne water Cherenkov neutrino detector in the Kamioka Mines in Japan, arrayed with photomultiplier tubes (*PMTs*), configured with a burst monitor for supernova neutrino bursts, and utilizing efficient false trigger rejection. It has a fiducial mass/“volume” of 32.5 ktonnes of ultra-pure water (Abe et al. 2016) and is, therefore, proton-rich. As such, it is most sensitive (Beck et al. 2013) to electron antineutrinos ($\bar{\nu}_e$) via super-allowed charged-current (CC) inverse beta decay (IBD) reaction:

$$\bar{\nu}_e + p \rightarrow e^+ + n, \quad (12)$$

which also boasts a low neutrino energy threshold of 1.8 MeV. Electron neutrinos and antineutrinos also interact via the charged-current absorption processes on Oxygen:

$$\nu_e + {}^{16}\text{O} \rightarrow e^- + {}^{16}\text{F} \quad (13)$$

and

$$\bar{\nu}_e + {}^{16}\text{O} \rightarrow e^+ + {}^{16}\text{N}. \quad (14)$$

The final state of CC interactions can also include neutrons and deexcitation gammas, and these are detectable. Detection of these secondaries can in principle be used to identify the interaction channel. Figure 1 depicts the suite of relevant cross sections for the detectors highlighted in this study, and, as indicated in the leftmost panel, that for

the IBD dwarfs those for the CC interactions on oxygen. All neutrino species interact via the neutral current (NC), and, thus, contribute to the signal via the measurement of a deexcitation gamma that accompanies the neutral-current excitation of resident nuclei in reactions such as:

$$\nu_i + {}^{16}\text{O} \rightarrow \nu_i + {}^{16}\text{O}^*. \quad (15)$$

All neutrino species scatter off electrons via the process:

$$\nu_i + e^- \rightarrow \nu_i + e^-, \quad (16)$$

but this process is subdominant. However, in this Compton-like process, the directionality of the incident neutrino is partially preserved, and this fact allows neutrino-electron scattering to be the dominant means, using neutrinos alone, to determine the direction of the supernova. As seen in Figure 1, the $\nu_e - e^-$ scattering cross section exceeds that for $\bar{\nu}_e - e^-$ scattering, and these are followed by those for $\nu_x - e^-$ scattering. In order to enhance its sensitivity to the IBD reaction and the associated secondary neutron, Super-K (and the follow-on Hyper-K, at ~ 250 ktonnes) might in the future be spiked with gadolinium (Beacom & Vagins 2004; Laha & Beacom 2014).

4.2 IceCube

IceCube is currently the largest neutrino observatory, with an effective mass of ~ 3.5 Mtonnes of pure water ice (Abbasi et al. 2011). Thus comprised of water, the suite of relevant neutrino-matter interactions is the same as in water Cherenkov detectors such as Super-K (§4.1). However, given its high energy threshold (above ~ 100 MeV), it is not currently capable of identifying individual supernova neutrino interactions, nor the energies of final-state electrons, gammas, or neutrons. Rather, the interaction of supernova neutrinos, predominantly by the IBD, will register in IceCube as a sudden increase in the background noise count rate. There are 5160 modules, each of which would detect the neutrino (mostly $\bar{\nu}_e$ s via the IBD) by the measurement in the phototubes of each module of the Cherenkov photons created by the neutrino's charged secondaries. The Cherenkov photon yield is $\sim 178\varepsilon_e$, where ε_e is the energy of the secondary positron or electron in MeV. This yields an effective volume per detector for the measurement of a single photon (on average and to compete with the noise in the module) of ~ 590 cubic meters at $\varepsilon_e \sim 20$ MeV (Köpke et al. 2011). Multiplying this number by 5160 yields an equivalent detector mass of ~ 2.8 Mtonnes. Since the sensitivity and signal yield of a supernova in IceCube depend upon numerous detector-specific systematics, such as angular sensitivity and absorption length, a Monte Carlo analysis of the detector capabilities, best performed by the IceCube team, is necessary. Therefore, for our purposes we will assume that the effective mass for 100% detection is 3.5 Mtonnes of water ice and the reader is encouraged to scale our theoretical signal rates to any updated effective mass.

For a galactic supernova, the sharp increase in the background rate over the short few-second time period associated with a supernova neutrino burst will be unmistakable. The background rate per detector module with a 0.25-millisecond deadtime setting is estimated to be ~ 286 Hertz (Köpke et

al. 2011)². It is assumed that the noise in these modules is uncorrelated and Poissonian. This yields a sigma for the collective background fluctuation of $\sim 1200\Delta t$, where Δt is the width of a time bin in seconds. This, together with the Poissonian fluctuation in the signal itself, sets the total noise floor (added in quadrature) against which to compare the average supernova signal to determine detectability. Since the Poissonian variation in the supernova signal goes as the square root of the signal, and, hence, inverse-linearly with distance, while the IceCube detector background is independent of distance, the overall noise level is dominated by the signal fluctuations at smaller distances (where the signal-to-noise will be large) and by the detector noise at large distances. This is not the case for the other detectors, for which there is effectively no background during a \sim second-long integration.

Nevertheless, IceCube, given its large effective mass, will be an excellent means to measure the neutrino- and neutrino-energy-integrated light curve. Therefore, though IceCube cannot provide event-by-event information, particle characterization, directionality, nor energy, it is still an exceptional detector for measuring the temporal development of the total neutrino flux. This can help constrain structures in the time signal such as accretion and cooling, and may provide good progenitor discrimination (see §6.2 and §6.3).

4.3 DUNE

The Deep Underground Neutrino Experiment (DUNE) is a ~ 40 -ktonne Liquid Argon Time Projection Chamber (LAr TPC) that is being built at the Sanford Laboratory in South Dakota's Homestake Mine (Acciarri et al. 2016). This class of detector has high sensitivity to electron neutrinos via the charged-current reaction:

$$\nu_e + {}^{40}\text{Ar} \rightarrow e^- + {}^{40}\text{K}^*, \quad (17)$$

which has a large per-nucleus cross section (see Figure 1) and a neutrino energy threshold of only 1.5 MeV (Botella 2016). DUNE will provide the best electron-neutrino light curve, and in fact will be the only detector to provide a high-statistics ν_e signal (Ankowski et al. 2016). Electron antineutrinos also interact with Argon via the charged current reaction:

$$\bar{\nu}_e + {}^{40}\text{Ar} \rightarrow e^+ + {}^{40}\text{Cl}^*. \quad (18)$$

This interaction's cross-section, as seen in Figure 1, is as much as two orders of magnitude smaller than that of its electron-neutrino counterpart. Of course, all species of neutrinos will contribute to the signal by elastically scattering off electrons. We do not in this study include neutral-current interactions in DUNE; there are still ongoing studies to determine the neutral-current interaction rates Argon, but these are currently unavailable in the SNOWGLOBES software (Kemp 2017; Beck et al. 2013). In a liquid argon

² This deadtime approach, along with the sampling rate that yielded a temporal resolution of ~ 2 milliseconds, may recently have been improved. Such changes will affect the per-module noise rate. However, for specificity and for the purposes of this study, we use the older detector characteristics as envisioned in Abbasi et al. (2011) and Köpke et al. (2011).

detector, the final-state charged particles deposit kinetic energy along an ionization trail in the liquid argon. In a TPC, a voltage is applied across the liquid argon to cause charges to drift towards the anode to be collected on wire planes. The times of arrival to the wire plane allow the three-dimensional tracks to be reconstructed. Individual articles can be identified by the rate of energy loss (Ankowski et al. 2016) and, therefore, DUNE is capable of resolving the energies of the final-state charged particles, from which the incident neutrino energy can be estimated. Without a tagging mechanism, the electrons from CC interactions cannot be distinguished from the elastically-scattered electrons, but the CC interaction on Argon has such a large cross section that it dominates the signal. In summary, DUNE will provide the most accurate estimates of the electron neutrino emissions of a core-collapse supernova.

4.4 JUNO

The Jiagmen Underground Neutrino Observatory is a Liquid Scintillator Antineutrino Detector currently under construction in Southern China. This neutrino detector will utilize ~ 20 kilotons of linear alkyl-benzene hydrocarbon scintillator, and employ 17,000 high-quantum-efficiency photomultiplier tubes (Grassi 2016). Its primary research objective is to study neutrino oscillations utilizing reactor-produced electron antineutrinos. However, like water-Cherenkov detectors, scintillator is proton-rich and is, therefore, sensitive to electron antineutrinos and the high-statistics IBD signal. In JUNO, scintillation light is emitted as charge particles as they lose energy in the medium, and that light is captured by PMT's. In addition to the IBD, charge-current absorption on carbon via reactions such as:

$$\nu_e + {}^{12}\text{C} \rightarrow e^- + {}^{12}\text{N} \quad (19)$$

$$\bar{\nu}_e + {}^{12}\text{C} \rightarrow e^+ + {}^{12}\text{B}. \quad (20)$$

contribute to the signal in the detector.

The charged-current interactions for the electron and anti-electron neutrinos have thresholds of 17.34 MeV and 14.39 MeV, respectively (An et al. 2015). As indicated in Figure 1, at 20 MeV the IBD cross section is ~ 40 times larger than that for the $\bar{\nu}_e - {}^{12}\text{C}$ CC interaction. As in other detectors, all neutrino species elastically scatter off of electrons. JUNO is capable of distinguishing the IBD reaction because its final-state neutrons will quickly capture on a proton and emit a 2.2 MeV gamma ray. Pulse-shape discrimination is used to distinguish electrons from positrons, thus allowing CC absorption and electron scattering to be distinguished (Franco et al. 2011). Neutral-current interactions with carbon:

$$\nu_i + {}^{12}\text{C} \rightarrow \nu_i + {}^{12}\text{C}^*, \quad (21)$$

involving all species are possible, and these produce observable deexcitation gammas, but JUNO will have limited sensitivity to them. However, JUNO should have good event-by-event energy resolution, though directional information will be difficult to acquire in the scintillator.

5 SUPERNOVA MODELS

Between Radice et al. (2017), Burrows et al. (2018), and Vartanyan et al. (2018), we calculated a collection of supernova models starting from the 9, 10, 11, 16, 17, 19, and 21 M_\odot progenitor models of Sukhbold et al. (2016) and integrated out to ~ 1 second after core bounce. The 1D variants did not explode, while the 2D variants did. These models, while not the final word, collectively capture the wide range of detailed model expectations for the neutrino emissions and signatures that have emerged from most recent theoretical work on the supernova mechanism. The multi-group radiation/hydrodynamic code FORNAX (Skinner et al. 2018; Burrows et al. 2018) was used with twenty energy groups for each neutrino species³. The radial coordinate, r , ran from 0 to 20,000 kilometers (km) in 608 zones (both 1D and 2D), while the polar angular grid spacing (in 2D) covered the full 180° and varied smoothly in 256 zones from $\approx 0.95^\circ$ at the poles to $\approx 0.65^\circ$ at the equator. We used the LS220 (Lattimer & Swesty 1991) nuclear equation of state (EOS) for the 9, 10, and 11 M_\odot models and the SFHo nuclear equation of state (Steiner et al. 2013) for the rest, the approximate general relativistic potential formalism of Marek et al. (2006), and GR redshifts were included in the transport. The many-body correction of Horowitz et al. (2017) was incorporated into the full collection of neutrino-matter interaction rates (Burrows, Reddy, & Thompson 2006) and inelastic scattering off electrons and nucleons as described in Burrows et al. (2018) was included. In the 2D simulations, seed perturbations were included in only the 10- M_\odot model (Radice et al. 2017), while numerical noise was allowed to seed the turbulence in the other 2D models. The products used to determine signals in underground detectors were the associated emergent luminosity spectra for each neutrino species as a function of time.

Quite generally, 1D and 2D emissions are similar until explosion. As previously stated, after explosion they differ due to the cessation of mass accretion onto the core at explosion, which is a major source of neutrino power. Qualitatively, the two sources of neutrino emission are diffusion from the core and accretion power. It is this transition to the phase of emission without accretion that distinguishes the exploding models, represented in this paper by the 2D models. Even if core collapse does not yield a supernova, and even if there is no optical counterpart, the neutrino signal from such a “failed” core will easily be observable throughout our galactic neighborhood in the collection of neutrino facilities we highlight in this paper. It is the differences between non-exploding models and exploding models (represented in this paper by 1D versus 2D models), due to the cessation of accretion in the latter, that we contend can be distinguished when the next neighborhood core collapse erupts.

As a copious literature shows (see Burrows 2013, and references therein), multi-D is crucial to explosion due to the turbulence behind the shock wave, turbulence that can be manifest only in 2D or 3D. However, until explosion and

³ For these simulations, we follow the ν_e , $\bar{\nu}_e$, and “ ν_μ ” species, where the four species, ν_μ , $\bar{\nu}_\mu$, ν_τ , and $\bar{\nu}_\tau$ are lumped together into “ ν_μ ”. For the ν_e types, the neutrino energy ϵ_ν varied logarithmically from 1 MeV to 300 MeV, while it varied from 1 MeV to 100 MeV for the $\bar{\nu}_{es}$ and $\nu_{\mu s}$.

the cessation of accretion, this turbulence has only modest effects on the overall neutrino emissions to infinity. Hence, before explosion, the neutrino emissions in 1D, 2D, and 3D simulations for a given progenitor are very similar. All models (1D, 2D, 3D) emit roughly like spheres - the multi-D variations due to turbulence washing out. The models in the sense of neutrino light curves are all pseudo-spherical. The role of multi-D is to introduce convection/turbulence to allow explosions by that agency and 2D and 3D neutrino emissions will be similar. The only difference expected between 2D and 3D models would be in the time of explosion, and, hence, in the time accretion stops and that component driving neutrino power, therefore, subsides. This will introduce only a quantitative difference between 2D and 3D, i.e. the time of explosion and the time of transition to diffusion power alone could be slightly different. In this paper, we are highlighting the qualitative differences between exploding and non-exploding models to identify a test of the theory that predicts this. Hence, the specific time of explosion is secondary to the thesis of our paper – the existence of the transition is primary. This has never before been falsified for a supernova model, making the detection of a neutrino burst and its time structure by the detection of events in underground laboratories a direct experimental test of supernova theory. Since calculating a multitude of 3D models is very expensive (each model can take a month or two to simulate on supercomputers), our 2D models are reasonable stand-ins for multi-D for the purposes of this paper.

We note that in our models we don't see any clear signs of a SASI (Blondin, Mezzacappa, & DeMarino 2003) modulation in the neutrino signal rates (Tamborra et al. 2014). That does not mean the SASI is not there, merely that the SASI is sub-dominant and obscured by the stronger neutrino-driven convection component. Specifically, we don't witness a near-monochromatic frequency modulation in the neutrino signal seen by some others (e.g., Tamborra et al. 2013,2014i; Kuroda et al. 2017). It may be that SASI-related signal modulations are associated with non-axisymmetric spiral modes seen in some non-exploding 3D simulations, and this possibility deserves further exploration. Such a feature would not be captured by our 2D models. However, in Burrows et al. (2012) and Vartanyan et al. (2018a), we argue that the SASI is clearly manifest only when the neutrino fluxes are too low to drive explosions, but when they are enough to lead to supernovae there is no clear tone, nor identifiable SASI feature in the neutrino signal rates. This, again, is what we see here, but the reader should note alternate points of view (Lund et al. 2010,2012).

Furthermore, we do not see the LESA phenomenon (Tamborra et al. 2014) in any of our simulations (see also Dolence et al. 2015). We speculate (but have not proven) that it is an artefact of the use of the ray-by-ray approach (Skinner et al. 2016), and have studied it extensively in both 2D and 3D (Vartanyan et al. 2018b, in preparation). Be that as it may, the LESA would merely result, if it existed, in an angular asymmetry in the neutrino lepton flux, and such an angular asymmetry is not observable from a single direction (i.e., when obtaining data only at Earth).

6 RESULTS

Table 1 summarizes the total number of events at 10 kiloparsecs (kpc) expected in all detectors during the first ~second after bounce for all models (both 1D and 2D) and for the three contexts of no-oscillation (NO), the normal hierarchy (NH), and the inverted hierarchy (IH). As expected, Ice-Cube should experience by far the largest number of events at 10 kpc, of order 10^5 , during this time interval, though it can not distinguish interaction channel nor neutrino energy nor type. Nevertheless, the entire galaxy should be within reach for all models, whether NH or IH obtains. The total signals in the other detectors during this earlier dynamical phase are still formidable and suggest that the entire galaxy is well within reach by them. As expected, among these the more massive facilities (such as Super-K, and later Hyper-K) boast the larger event yields. At the low progenitor mass end, the 1D and 2D models yield roughly similar integrated event yields (though different light curves in detail). This is due to the earlier explosion times post-bounce of such progenitors and to their steeper density profiles. The latter translates into a more rapid decrease in the accretion rate and, hence, the accretion powered neutrino luminosity, before explosion, so that the accretion-powered phase is both weaker and shorter-lived. Diffusion from the core then starts to ascend in relative importance.

Figures 2, 3, and 4 provide the energy luminosities and RMS neutrino energies for all models (both 1D [dashed] and 2D [solid]) and neutrino species and for the no-oscillation, normal-hierarchy, and inverted-hierarchy cases. These curves depict input quantities before convolution in the various detectors, but after our oscillation model operates (if it does). The no-oscillation numbers are what the supernova models give and the NH and IH numbers reflect the result of applying the oscillation model described in §3. For higher-mass progenitors, the corresponding event yields from the 2D (exploding) models should be generally lower than those for the 1D models. In these cases, the continuation of significant accretion due to the failure in 1D to explode translates into higher neutrino luminosities for longer times. In addition, the average and root-mean-square (RMS) neutrino energies of the more massive progenitors at the later times are slightly higher than their corresponding 2D counterparts. The upshot should be significantly higher event rates for the 1D models at later times for the progenitors with shallow mass density profiles (high “compactness”; O’Connor & Ott 2011,2013). We suggest that the distinctly different event light curves for 1D and 2D, particularly for the higher compactness models (mostly for higher progenitor mass, with exceptions), reflect in a generic sense the difference between non-exploding and exploding models. Factors of more than two in the event rates at later times (after hundreds of milliseconds) are possible. Note that one expects the temporal fluctuations in the event rates and inferred neutrino luminosities for the 2D (exploding) models to be larger than in the 1D cases. This is a consequence of turbulence in the multi-D models (impossible in 1D) and the associated episodic nature of plume accretion onto the PNS core before, during, and just after explosion when asphericities are allowed. Fluctuations in the energy luminosities of as much as ~25% on timescales of ~10 to ~100 milliseconds are seen. The detection of such temporal structures could be

used to constrain post-bounce and post-explosion accretion rate variations in angle and time.

6.1 Neutrino Light Curves

Figures 5, 6, 7, and 8 portray the total all-channel event rates in the Super-K, DUNE, JUNO, and IceCube detectors, respectively, for the 10 M_{\odot} and 19 M_{\odot} models, for both 1D and 2D realizations, and for all neutrino oscillation assumptions. Such plots allow one to focus on both the differences between low-mass and higher-mass light curves and on the differences as a function of neutrino hierarchy.

Since Super-K is most sensitive to $\bar{\nu}_e$ s, as Figure 5 suggests, the high signal rate in the NO (no-oscillation) case is muted in either oscillation model. For the 1D (non-exploding) case, the differences in event rate can be large, as much as $\sim 40\%$ for the low-mass progenitor and more than a factor of two for the higher-mass progenitor, but for the two 2D (exploding) models the differences between the various oscillation models in the corresponding light curves are smaller. For the exploding (2D) models, unlike in the non-exploding models (particularly for the higher progenitor mass) the largest differences between the various oscillation assumptions are at earlier post-bounce times within a few hundred milliseconds. At the later times, the NH and IH signal rates get closer. As Figure 5 suggests, during the first hundreds of milliseconds, there is generically an accretion luminosity hump that evinces a large post-bounce and post-breakout signal rate. For the low-mass progenitor this hump in 1D decays quickly (with an “e-folding” time near ~ 0.8 seconds), but for the higher-mass progenitor the 1D signal drops and then rises or flattens. For this 19- M_{\odot} progenitor, the drop is due to the accretion of the silicon/oxygen interface and the associated drop in mass flux at the shock, while the rise for the NO case and the near-flattening for the NH and IH cases are due to the fact that accretion continues in a non-exploding model and the average and RMS neutrino energies continue to grow (see Figures 2, 3, and 4) as the core contracts and the neutrinospheres compressionally heat. The neutrino-matter cross sections in detectors increase with neutrino energy (Figure 1). So, for higher-mass exploding (2D) models, the accretion of the silicon/oxygen interface results in a decrease in the event rate, but this decrease is less manifest due to the almost simultaneous explosion and reversal of net accretion. For the lower-mass progenitors, the magnitude of the density drop at this interface is smaller and explosions can occur before it, or a similar structure, is accreted (Radice et al. 2017). Hence, the accretion powered phase, the accretion of the silicon/oxygen interface itself, the progenitor-model and/or compactness (seen mostly through the overall event rate), and the explosion/no-explosion dichotomy are all in principle observables (Horiuchi et al. 2017). The NH and IH hierarchies are less easily discerned in Super-K, though the earlier breakout burst is rather different for the two scenarios (Wallace et al. 2016).

On the other hand, DUNE (Figure 6), sensitive as it is to ν_e s, manifests at early post-bounce times an inversion in the event rate ordering for the NO, NH, and IH situations vis à vis Super-K for both the 10- M_{\odot} and 19- M_{\odot} . In Super-K, the early event rates around the hump are in the order NO > NH > IH for both non-exploding and exploding

models, but in DUNE they are NH > IH > NO. After ~ 200 milliseconds, in both the 10- M_{\odot} and 19- M_{\odot} non-exploding models this order reverses, and is NO > IH > NH. So, for the non-exploding models and at later times, the NH/IH order reverses in DUNE relative to the behavior in Super-K. For the exploding (2D) models, the event rate differences between the hierarchies are smaller. However, we note that at the earlier times (< 200 milliseconds after bounce) the light curve shapes in DUNE and Super-K are very different, reflecting their differential neutrino flavor sensitivities. This, along with a potential capacity in each detector to discriminate channel, flavor, and spectra, could be used to derive both oscillation modality and progenitor-model constraints. We emphasize, as do Wallace et al. (2016), and as is suggested via Figure 6 and Figures 10 and 14 below, that DUNE’s ν_e sensitivity makes it the best detector of the four highlighted in this paper to discern the breakout burst, and with it to distinguish the normal from the inverted hierarchy.

As Figures 5, 7, & 8 demonstrate, due to the $\bar{\nu}_e$ sensitivity in all three, the light curves in JUNO, IceCube, and Super-K are qualitatively similar. IceCube, however, if the fiducial volume we have assumed for it obtains, would experience a much higher rate of signal accumulation⁴. Nevertheless, the temporal structure of the neutrino burst during the dynamical supernova phase is best discerned via IceCube, but the flavor and spectral character of the burst can be determined clearly only via the channel and event energy discrimination that might be possible in the collective combination of Super-K, DUNE, and JUNO. The differential sensitivity of Super-K and JUNO on the one hand and DUNE on the other vis à vis $\bar{\nu}_e$ s and ν_e s will be particularly revealing. As noted, we have focused in this paper on all-channel energy-integrated rates and defer a discussion of the spectral and channel capabilities in these three detectors (and in Hyper-K) to a later paper.

In Figures 9, 10, 11, and 12, we present all the all-channel light curves for all the progenitors studied, for both 1D (non-exploding) and 2D (exploding) realizations in Super-K, DUNE, JUNO, and IceCube. The basic systematics with progenitor articulated and described above using only the 10- M_{\odot} to 19- M_{\odot} models survives. The wide range of signal rates as a function of progenitor mass and compactness is clear. For the non-exploding models, the early-time event rates can vary by a factor of ~ 2 , while the late-time event rates can vary by a factor of ~ 10 for the non-oscillating case and ~ 5 for the oscillating cases. For the exploding models, variations of at least a factor of ~ 2 are expected from 9- M_{\odot} to 21- M_{\odot} . Since a galactic supernova will almost certainly be measured electromagnetically, the distance to the supernova will be known. Given the distance, the absolute flux and fluence can be determined and with it some measure of the core structure/compactness of the progenitor. The electromagnetic data will likely reveal the progenitor mass, so the absolute neutrino signal can be paired with the progenitor star to constrain stellar evolution and supernova models together.

⁴ At 10 kiloparsecs, a CCSN would register during the first second of post-bounce evolution $\sim 10^4$ times as many events in IceCube as were culled by Kamioka II from SN 1987A. The other detectors highlighted here would witness $\sim 10^2$ times more events.

6.2 Detection Ranges and Feature Measurement

We emphasize that a detected signal will be in our galaxy, or in very local environs (such as the LMC or SMC). Given this, the distance to the supernova (and most probably the progenitor mass and photon luminosity) will be known via its electromagnetic counterparts. Hence, there is no distance degeneracy for exploding models. This allows us readily to distinguish the signal rate levels for the various progenitors and to experimentally test the models. With a distance (and perhaps an electromagnetically-derived progenitor mass), the detection of the neutrino signals in the various detectors described will provide excellent constraints on and insights into supernova theory and on the models we use here (Radice et al. 2017; Vartanyan et al. 2018a; Burrows et al. 2018).

Table 1 provides the total number of events expected at 10 kiloparsecs in all the models and for all the detectors studied. For Super-K, DUNE, and JUNO the effective background count rate is negligible during times of order one second. Therefore, if we assume Poisson statistics for the signal fluctuations, deriving the total number of events to $\sim 10\%$ accuracy at $1\text{-}\sigma$ would require that $\frac{1}{\sqrt{N}} \sim 0.1$, where N is the number of events. This criterion yields $N \sim 100$, and, therefore, a range of ~ 100 kiloparsecs for these three detectors. This encompasses the entire Milky Way and the Magellanic Clouds. However, an accuracy of 10% for the entire signal during the dynamical “first second” is not that impressive. Astronomers would want to discern various temporal structures, such as the post-bounce accretion hump. Using Figures 5–7 and 9–11, we can determine that to capture the number fluence during the accretion hump (assuming that it lasts for ~ 200 milliseconds) to at least $\sim 10\%$ accuracy the distance of the supernova needs to be closer than 20 to 25 kpc for Super-K and ~ 10 to 15 kpc for DUNE, depending upon oscillation and progenitor model. This still encompasses most of the Milky Way. The corresponding numbers for JUNO are in most cases in between. In general, and approximately, in order to discern a temporal feature, “ i ”, of width Δt whose average signal rate is $\dot{E}_i (= \frac{dN_{det}}{dt})$ to within a fraction, f , requires that $f > N_i^{-1/2} \sim \frac{1}{(\dot{E}_i \Delta t)^{1/2}}$. For example, to identify a temporal fluctuation in the event rate of 10% that might occur over a Δt of 10 milliseconds requires a “background” \dot{E}_i of $\sim 10,000$ Hertz. In Super-K, the higher-mass progenitors need to be within $\sim 5\text{--}6$ kpc to achieve this, depending upon oscillation model and epoch of fluctuation. Such fluctuations might arise due to episodic accretion or rotation and would usefully constrain the character of the turbulence in the core and behind the shock wave. A feature with a larger Δt would be discernible out to a correspondingly greater distance. In fact, the range out to which one could discern a fluctuation f of duration Δt is proportional to f and $\sqrt{\Delta t}$. Hence, to capture a small fluctuation of 1% over an interval of 10 milliseconds would require a supernova distance below ~ 1 kpc for most models. Only of order 1% of the galaxy is within this distance.

Nevertheless, as Figures 5–7 and 9–11 clearly demonstrate, the general evolution of the neutrino light curve during the crucial dynamical supernova phase will be accessible for a core-collapse supernova going off in most of our galaxy. Moreover, as Figures 9–11 reveal, the range of event rates as a function of progenitor can vary by a factor of two to five, depending upon whether the model explodes and, to some

degree, upon whether the in Super-K, DUNE, and JUNO for supernovae throughout the galaxy. For instance, for the normal hierarchy and non-exploding models, the $9\text{-}M_\odot$ and $10\text{-}M_\odot$ progenitor predictions can be distinguished in Super-K out to ~ 100 kpc. For the exploding models, the variation in signal rate is approximately a factor of two and the $\sim 25\%$ variation from model to model seen in this model suite can be resolved out to $50\text{--}100$ kpc. Of course, more precise discrimination requires closer supernovae, but the numbers for the parameter examples given are already rather impressive.

IceCube has a significant background count rate. The supernova would be identified by a rise in this background. If we assume a background of $1200 \Delta t$ Hertz (§4.2), then the signal to background ratio for the first second after collapse ranges from ~ 100 to ~ 300 at 10 kpc. This implies that a supernova anywhere in the Milky Way could be detected in IceCube. Since the Poissonian noise fluctuation of the signal itself binned in 10-millisecond bins exceeds that in the detector for distances less than $\sim 3\text{--}5$ kpc, the signal in IceCube will be detector-noise-limited for much of the galaxy. At a signal rate (\dot{E}) of $\sim 10^5$ Hertz, the signal-to-background ratio is ~ 9 for $\Delta t = 10$ milliseconds and ~ 4 for $\Delta t = 2$ milliseconds. At an \dot{E} of $\sim 3 \times 10^5$, the corresponding numbers are ~ 27 and ~ 12 . Therefore, at the higher rate (see Figure 12), IceCube should be able to measure the event rate in 10-millisecond bins to $\sim 4\%$, and in 20-millisecond bins to $\sim 3\%$. This would enable exquisite model discrimination at 10 kpc. Within a given oscillation paradigm, IceCube is able to discriminate the various progenitors for any galactic CCSN solely on the basis of the general level of flux measured. Hence, with $\sim 10^2$ times the signal rate found in the other detectors, it should be able to achieve for a time bin of 10 milliseconds and distances less than ~ 5 kpc (approximately interior to which the signal noise exceeds the detector noise) ~ 10 times the precision in the estimation of instantaneous event rate (ten times smaller f s). Hence, IceCube will be able to provide exquisite all-channel neutrino light curves throughout most of the galaxy.

Doing a full MCMC or Bayesian analysis to determine significance is beyond the scope of this paper, which has, as discussed, much more limited ambitions. However, we provide in Figures 13 and 14 neutrino light curves that include Poissonian error bars at 10 kiloparsecs and for time bins of 50 milliseconds for Super-K and DUNE for the suite of mass models from 9 to 21 solar masses and in the NH and IH contexts. This enables one to gauge the ability of these detectors to separate out the various masses. As can be seen from Figures 13 and 14, the model discrimination capability of these detectors interior to ~ 10 kiloparsecs is rather good. Time binning is at the discretion of those performing the data analysis, so had we used in Figures 13 and 14 even coarser binning the capacity to discriminate models within our galaxy would have been demonstrated to be even better.

In Table 2, we provide the ranges for Super-K, JUNO, and DUNE at which the signal-to-noise ratio is five for a measurement of the flux at the first post-bounce peak, centered in a 10-ms bin around that time. We do this for all models and for both the Normal and Inverted hierarchies. This procedure can be applied to any light-curve feature, and the results depicted in Table 2 are merely representative. Nevertheless, Table 2 gives the reader a quantitative estimate of the supernova ranges out to which an impor-

tant light-curve feature could be discerned by an important subset of current and near-term underground neutrino observatories.

6.3 Temporal Feature Registration

If a measurement is signal Poisson-limited (as it is for Super-K, DUNE and JUNO), the precision with which a temporal feature (a hump or fluctuation) can be registered in time goes roughly as the feature width, Δt , divided by the square root of the event number, N_i , under the feature. This is the “centroiding” problem and implies that the distance out to which one can time-register a feature scales with the feature width⁵. If the feature has a width of 10 milliseconds, it will require $N_i \sim 100$ to register the feature to within ~ 1 millisecond. As Wallace et al. (2016) have shown, to determine the peak time of the ν_e breakout burst to within ~ 1 millisecond in the inverted hierarchy requires a supernova at a distance of less than ~ 4 kpc. For the normal hierarchy, the breakout burst is much less easily captured (see §3). However, for a given underlying model, the huge number of events expected during the subsequent dynamical phase would enable better fractional registration of longer duration features. For instance, using Super-K data, centroiding the accretion hump of ~ 200 millisecond duration for the exploding $19-M_\odot$ progenitor to within ~ 10 milliseconds could in principle be done out to a range of ~ 10 kpc. For context, the mean time between single events during the SN 1987A campaign was ~ 1 second.

We note that when a black hole forms, the neutrino signal should immediately shut off (Burrows 1984). This would be a precipitous drop, effectively an edge, and a detector’s capacity to determine the precise time of black hole formation will be limited by the instantaneous event rate just before that time. Though for this paper we did not simulate the neutrino light curve for black hole formation, the event rates provided for the 1D models in the relevant figures are indicative of the approximate rates when such a secondary collapse to a black hole would occur. Using these numbers suggests that the time of black hole formation could be determined in Super-K, DUNE, or JUNO to one millisecond out to 10–20 kpc.

7 CONCLUSIONS

Most of the neutrino burst signal diagnostic of supernova dynamics and the hydrodynamics of core-collapse occurs in this first \sim second after core bounce. However, most of the signal occurs later during the subsequent tens-of-seconds of PNS cooling and deleptonization (Burrows & Lattimer 1986). Nevertheless, the neutrino light curve, spectral evolution, and species mix during this first crucial phase uniquely bear the stamp of the internal dynamics of the supernova. In this paper, we have presented models of the all-channel neutrino light curve (event-rate/signal evolution) in four current and planned underground neutrino detectors for seven exploding and non-exploding progenitor models, with and

without neutrino oscillations, in order to quantify the systematic variations of the neutrino event rate evolution with progenitor mass, oscillation model, and whether the model exploded. We identify features in the light curves diagnostic of each, as well as of the pre-collapse core mass density profile, the accretion of the silicon/oxygen interface, and temporal variations due to episodic accretion events. The network of large-volume neutrino detectors that is emerging around the world will be hugely capable of constraining, perhaps in detail, the evolution in real time of the supernova phenomenon for any galactic core-collapse supernova and providing much-needed ground truth for the theory of supernovae upon which so many have labored these last five decades⁶.

ACKNOWLEDGEMENTS

The authors acknowledge support under U.S. NSF Grant AST-1714267 and the Max-Planck/Princeton Center (MPPC) for Plasma Physics (NSF PHY-1144374), and by the DOE SciDAC4 Grant DE-SC0018297 (subaward 00009650). DR acknowledges support as a Frank and Peggy Taplin Fellow at the Institute for Advanced Study. In addition, this material is based upon work supported by the U.S. Department of Energy, Office of Science, Office of Advanced Scientific Computing Research, and the Scientific Discovery through Advanced Computing (SciDAC) program under Award Number DE-SC0018297 (subaward 00009650). The authors employed computational resources provided by the TIGRESS high performance computer center at Princeton University, which is jointly supported by the Princeton Institute for Computational Science and Engineering (PICSciE) and the Princeton University Office of Information Technology, and by the National Energy Research Scientific Computing Center (NERSC), which is supported by the Office of Science of the US Department of Energy (DOE) under contract DE-AC03-76SF00098. The authors express their gratitude to Ted Barnes of the DOE Office of Nuclear Physics for facilitating their use of NERSC.

REFERENCES

- Abbasi, R. et al. 2011, *A&A*, 535, A109
- Abe, K. et al. 2011, arXiv:1109.3262
- Abe, K. et al. 2016, *Astropart. Phys.*, 81, 39
- Abe, K. et al. 2018, *Hyper-Kamiokande: Design Report*, arXiv:1805.04163
- Acciarri, R., Acero, M.A., Adamowski, M., et al. 2016, arXiv:1601.02984
- An, F., An, G., An, Q., et al. 2016, *Journal of Physics Nuclear Physics G*, 43, 030401
- Ankowski, A. et al., “Supernova Physics at DUNE,” in *Supernova Physics at DUNE*, Blacksburg, Virginia, USA, March 11-12, 2016, arXiv:1608.07853
- Beacon, J.F. & Vagins, M.R. 2004, *Phys. Rev. Lett.*, 93, 171101
- Beck, A. et al. 2013, “Snowglobes”, <http://phy.duke.edu/~schol/snowglobes/>
- Bethe, H. & Wilson, J.R. 1985, *ApJ*, 295, 14

⁵ This is a very approximate statement of the more general Cramer-Rao theorem (Hogg & Craig 1978).

⁶ All of the models calculated in this paper are available upon request.

- Bionta, R.M. et al. 1987, *Phys. Rev. Lett.*, 58, 1494
- Blondin, J.M., Mezzacappa, A., & DeMarino, C. 2003, *ApJ*, 584, 971 (astro-ph/0210634)
- Burrows, A. 1984, *ApJ*, 283, 848
- Burrows, A. & Lattimer, J.M. 1986, *ApJ*, 307, 178
- Burrows, A. & Lattimer, J.M. 1987, *ApJ*, 318, L63
- Burrows, A. 1988, *ApJ*, 334, 891
- Burrows, A. 1990, *Ann. Rev. Nucl. Part. Sci.*, 40, 181
- Burrows, A., Klein, D., & Gandhi, R. 1992, *Phys. Rev. D*, 45, 3361
- Burrows, A., Hayes, J., & Fryxell, B.A. 1995, *ApJ*, 450, 830
- Burrows, A., Reddy, S., & Thompson, T.A. 2006, *Nuclear Physics A*, 777, 356-394
- Burrows, A., Dolence, J.C., & Murphy, J. 2012, *ApJ*, 759, 5 (arXiv:1204.3088)
- Burrows, A. 2013, *Reviews of Modern Physics*, 85, 245
- Burrows, A., Vartanyan, D., Dolence, J.C., Skinner, M.A., & Radice, D. 2018, *Space Science Reviews*, 214, 33 (arXiv:1611.058959)
- Capozzi, F., Valentino, F., Lisi, E., Marrone, A., Melchiorri, A., & Palazzo, A. 2017, *Phys. Rev. D*, 95, 096014
- Dasgupta, B., O'Connor, E., & Ott, C.D. 2012, *Phys. Rev. D*, 85, 065008 (arXiv:1106.1167)
- Dighe, A.S. & Smirnov, A.Y. 2000, *Phys. Rev. D*, 62, 033007
- Dolence, J., Burrows, A., & Zhang, W. 2015, *ApJ*, 800, 10 (arXiv:1403.6115)
- Duan, H., Fuller, G.M., & Qian, Y.-Z. 2006, *Phys. Rev. D*, 74, 123004 (astro-ph/0511275)
- Fischer, T., Whitehouse, S.C., Mezzacappa, A., Thielemann, F.-K., Liebendörfer, M. 2009, *A&A*, 499, 1
- Franco, D., Consolati, G., & Trezzi, D. 2011, *Phys. Rev. C*, 83, 015504
- Gallo Rosso, A., Vissani, F., & Volpe, M.C. 2018, *J. Cosmology Astropart. Phys.*, 4, 040, arXiv:1712.05584
- Grassi, M. 2016, Proceedings for the XIII International Conference on Heavy Quarks and Leptons (HQL2016), 22- 27 May, 2016, Blacksburg, Virginia, USA. <http://pos.sissa.it/cgi-bin/reader/conf.cgi?confid=274>, id.73, 73
- Hirata, K. et al. 1987, *Phys. Rev. Lett.*, 58, 1490
- Hirschi, R., Meynet, G., & Maeder, A. 2005, *A&A*, 425, 649-670
- Hogg, R.V. & Craig, A.T. 1978, *Introduction to Mathematical Statistics*, 4th Edition (Macmillan, New York)
- Horiuchi, S., Nakamura, K., Takiwaki, T., & Kotake, K. 2017, arXiv:1708.08513
- Horiuchi, S. & Kneller, J.P. 2017, arXiv:1709.01515
- Horowitz, C.J. 2002, *Phys. Rev. D*, 65, 043001
- Horowitz, C.J., Caballero, O.L., Lin, Z., O'Connor, E., & Schwenk, A. 2017, *Phys. Rev. C*, 95, 025801 (arXiv:1611.05140)
- Hubber et al. 2010
- Janka, H.-T., & Müller, E. 1996, *A&A*, 306, 167
- Kato, C., Nagakura, H., Furusawa, S., et al. 2017, *ApJ*, 848, 48
- Kawagoe, S., Yoshida, T., Kajino, T., et al. 2010, *Phys. Rev. D*, 81, 123014
- Kemp, E. 2017, *Astronomische Nachrichten*, 338, 993
- Köpke, L. et al. 2011, Contribution to the "5th Symposium on Large TPCs for Low Energy Rare Events and Workshop on Neutrinos from Supernovae," Paris, Dec. 16-17, 2010, arXiv:1106.6225
- Kuroda, K., Kotake, K., Hayama, K., & Takiwaki, T. 2017, *ApJ*, 851, 62 (arXiv:1708.05252)
- Laha, R. & Beacom, J.F. 2014, *Phys. Rev. D*, 89, 063007
- Lattimer, J.M., & Swesty, F. D. 1991, *Nucl. Phys.*, A535, 331
- Liao, W. 2016, *Phys. Rev. D*, 84, 113016
- Lu, J.-S., Cao, J., Li, Y.-F., & Zhou, S. 2015, *JCAP*, 5, 0044
- Lund, T., Marek, A., Lunardini, C., Janka, H.-T., & Raffelt, G. 2010, *Phys. Rev. D*, 82, 063007
- Lund, T., Wongwathanarat, A., Janka, H.-T., Müller, E., & Raffelt, G. 2012, *Phys. Rev. D*, 86, 105031
- Maeder, A. & Meynet, G. 2012, *Rev. Mod. Phys.*, 84, 25-63
- Marek, A., Dimmelmeier, H., Janka, H.-T., Müller, E., & Buras, R. 2006, *A&A*, 445, 273
- Mirizzi, A., Tamborra, I., Janka, H.-T., Saviano, N., Scholberg, K., Bollig, R., Hüdepohl, L., & Chakraborty, S. 2016, *Nuovo Cimento*, 39, 1-112 (arXiv:1508.00785)
- Morozova, V., Radice, D., Burrows, A. & Vartanyan, D. 2018, submitted to *ApJ*(arXiv:1801.01914)
- Müller, B., & Janka, H.-T. 2014, *ApJ*, 788, 82 (arXiv:1402.3415)
- Nakamura, K., Horiuchi, S., Tanka, M., Hayama, K., Takiwaki, T., & Kotake, K. 2016, *MNRAS*, 461, 3296 (arXiv:1602.03028)
- Nikrant, A., Laha, R., & Horiuchi, S. 2018, *Phys. Rev. D*, 97, 023019
- Nomoto, K. & Hashimoto, M. 1988, *Physics Reports*, 163, 13
- E. O'Connor, C.D. Ott, *ApJ*730, 70 (2011)
- E. O'Connor, C.D. Ott, *ApJ*762, 126 (2013)
- Pantaleone, J.T. 1992, *Phys. Rev. D*, 46, 510
- Radice, D., Burrows, A., Vartanyan, D., Skinner, M.A., Dolence, J.C. 2017, *ApJ*, 850, 43 (arXiv:1702.03927)
- Sarikas, S., Raffelt, G., Hüdepohl, L., & Janka, H.-T. 2012, *Phys. Rev. Lett.*, 108, 061101 (arXiv:1109.3601)
- Scholberg, K. 2012, *Ann. Rev. Nucl. Part. Sci.*, 62, 81
- Scholberg, K. 2018, *Journal of Physics G Nuclear Physics*, 45, 014002 (arXiv:1707.06384)
- Serpico, P. D., Chakraborty, S., Fischer, T., et al. 2012, *Phys. Rev. D*, 85, 085031
- Skinner, M.A., Burrows, A., & Dolence, J. 2016, *ApJ*, 831, 81 (arXiv:1512.00113)
- Skinner, M.A., Dolence, J.C., Burrows, A., Radice, D. & Vartanyan, D. 2018, in preparation
- Steiner, A.W., Hempel, M., & Fischer, T., *ApJ*, 774, 17 (2013).
- Sukhbold, T., Ertl, T., Woosley, S.E., Brown, J.M., & Janka, H.-T. 2015, *ApJ*, 821, 38
- Sumiyoshi, K., Yamada, S., Suzuki, H., & Chiba, S. 2006, *Phys. Rev. Lett.*, 97, 091101
- Tamborra, I., Hanke, F., Müller, B., Janka, H.-T., & Raffelt, G. 2013, *Physical Review Letters*, 111, 121104
- Tamborra, I., Raffelt, G., Hanke, F., Janka, H.-Th., & Müller, B. 2014, *Phys. Rev. D*, 90, 045032 (arXiv:1406.0006)
- Thompson, T.A., Burrows, A., & Pinto, P. 2003, *ApJ*, 592, 434
- Vartanyan, D., Burrows, A., Radice, D., Skinner, M.A., & Dolence, J.C. 2018a, accepted to *MNRAS*(arXiv:1801.08148)
- Wallace, J., Burrows, A., & Dolence, J. 2016, *ApJ*, 817, 182
- Woosley, S.E., Heger, A., & Weaver, T.A. 2002, *Rev. Mod. Phys.*, 74, 1015
- Woosley, S. E., & Heger, A. 2007, *Phys. Rep.*, 442, 269

Table 1. Total number of events for a given progenitor for various detectors at 10 kiloparsecs during the earlier “supernova” dynamical phase. We provide the total number of accumulated events within our calculational time near ~ 1 second, starting at 50 ms before bounce and ending near as long as ~ 950 ms after bounce. These terminal times after bounce are given in the table heading. NO stands for “no oscillation”, NH stands for “normal hierarchy”, and IH stands for “inverted hierarchy”.

| | 9 M_{\odot} | | 10 M_{\odot} | | 11 M_{\odot} | | 16 M_{\odot} | | 17 M_{\odot} | | 19 M_{\odot} | | 21 M_{\odot} | |
|--------------|----------------|----------------|----------------|----------------|----------------|----------------|----------------|----------------|----------------|----------------|----------------|----------------|----------------|----------------|
| | 1D (778 ms) | 2D (950 ms) | 1D (838 ms) | 2D (950 ms) | 1D (887 ms) | 2D (616 ms) | 1D (942 ms) | 2D (950 ms) | 1D (944 ms) | 2D (950 ms) | 1D (937 ms) | 2D (950 ms) | 1D (928 ms) | 2D (950 ms) |
| Super-K (NO) | 1057 | 1143 | 2114 | 1743 | 2100 | 1163 | 3449 | 2092 | 3683 | 2278 | 4652 | 2573 | 3402 | 1971 |
| Super-K (NH) | 880 | 1096 | 1600 | 1591 | 1401 | 1002 | 2184 | 1716 | 2321 | 1870 | 2837 | 2112 | 2147 | 1642 |
| Super-K (IH) | 815 | 1076 | 1452 | 1528 | 1223 | 947 | 1879 | 1585 | 1996 | 1724 | 2431 | 1944 | 1844 | 1526 |
| DUNE (NO) | 471 | 476 | 1200 | 817 | 1244 | 534 | 2182 | 1011 | 2345 | 1132 | 3060 | 1275 | 2155 | 949 |
| DUNE (NH) | 485 | 620 | 897 | 929 | 711 | 552 | 1099 | 946 | 1168 | 1048 | 1413 | 1193 | 1077 | 910 |
| DUNE (IH) | 475 | 529 | 1083 | 859 | 1041 | 542 | 1762 | 987 | 1888 | 1102 | 2417 | 1247 | 1737 | 936 |
| JUNO(NO) | 852 | 933 | 1652 | 1423 | 1643 | 948 | 2662 | 1701 | 2837 | 1852 | 3550 | 2093 | 2625 | 1611 |
| JUNO (NH) | 715 | 906 | 1249 | 1311 | 1096 | 827 | 1672 | 1409 | 1772 | 1534 | 2136 | 1732 | 1643 | 1357 |
| JUNO (IH) | 661 | 885 | 1128 | 1255 | 950 | 779 | 1425 | 1300 | 1508 | 1414 | 1804 | 1594 | 1398 | 1259 |
| IceCube (NO) | 113854 | 123084 | 227649 | 187727 | 226195 | 125254 | 371439 | 225329 | 396647 | 245295 | 501013 | 277047 | 366332 | 212280 |
| IceCube (NH) | 94815 | 118007 | 172308 | 171384 | 150855 | 107922 | 235201 | 184820 | 249963 | 201397 | 305563 | 227457 | 231191 | 176868 |
| IceCube (IH) | 87733 | 115928 | 156345 | 164540 | 131685 | 102004 | 202312 | 170721 | 215008 | 185686 | 261827 | 209335 | 198581 | 164353 |

Table 2. Ranges (in kpc) for the determination at $5\text{-}\sigma$ of the neutrino event rate for a 10-ms bin centered on the first peak following breakout for both the Normal and Inverted hierarchies. This is usually associated with the accretion-powered phase, but for DUNE, given that the signal in it is dominated by the ν_e component at Earth, the peak times for a give model do not match those in the corresponding neutrino light curves in Super-K, JUNO, and IceCube. Times at which the bins are centered for Super-K and JUNO are given in the heading and for DUNE in the body of the Table.

| | 9 M_{\odot} | | 10 M_{\odot} | | 11 M_{\odot} | | 16 M_{\odot} | | 17 M_{\odot} | | 19 M_{\odot} | | 21 M_{\odot} | |
|--------------|----------------|----------------|----------------|----------------|----------------|----------------|----------------|---------------|----------------|----------------|----------------|----------------|----------------|---------------|
| | 1D (109 ms) | 2D (101 ms) | 1D (164 ms) | 2D (124 ms) | 1D (131 ms) | 2D (113 ms) | 1D (112 ms) | 2D (96 ms) | 1D (118 ms) | 2D (103 ms) | 1D (153 ms) | 2D (105 ms) | 1D (76 ms) | 2D (76 ms) |
| Super-K (NH) | 9.60 | 9.35 | 10.61 | 10.01 | 10.27 | 9.90 | 11.25 | 10.88 | 11.62 | 11.20 | 12.51 | 11.81 | 10.91 | 10.73 |
| Super-K (IH) | 9.01 | 8.83 | 9.93 | 9.47 | 9.58 | 9.30 | 10.52 | 10.26 | 10.86 | 10.55 | 11.59 | 11.10 | 10.30 | 10.18 |
| JUNO (NH) | 8.70 | 8.48 | 9.59 | 9.09 | 9.30 | 8.98 | 10.19 | 9.88 | 10.53 | 10.16 | 11.26 | 10.71 | 9.89 | 9.74 |
| JUNO (IH) | 8.16 | 8.00 | 8.98 | 8.59 | 8.68 | 8.43 | 9.53 | 9.30 | 9.83 | 9.57 | 10.45 | 10.06 | 9.33 | 9.22 |
| | (113 ms) | (112 ms) | (170 ms) | (116ms) | (134 ms) | (114 ms) | (115 ms) | (106 ms) | (120 ms) | (110 ms) | (157 ms) | (112 ms) | (79 ms) | (81 ms) |
| DUNE (NH) | 6.89 | 6.69 | 7.85 | 7.23 | 7.43 | 7.11 | 8.20 | 7.90 | 8.51 | 8.15 | 9.28 | 8.628 | 7.88 | 7.75 |
| | (153 ms) | (112 ms) | (170 ms) | (168 ms) | (134 ms) | (127 ms) | (115 ms) | (106 ms) | (120 ms) | (118 ms) | (157 ms) | (145 ms) | (79 ms) | (81 ms) |
| DUNE (IH) | 6.65 | 6.36 | 7.83 | 7.03 | 7.25 | 6.88 | 7.86 | 7.50 | 8.22 | 7.81 | 9.46 | 8.50 | 7.18 | 7.10 |

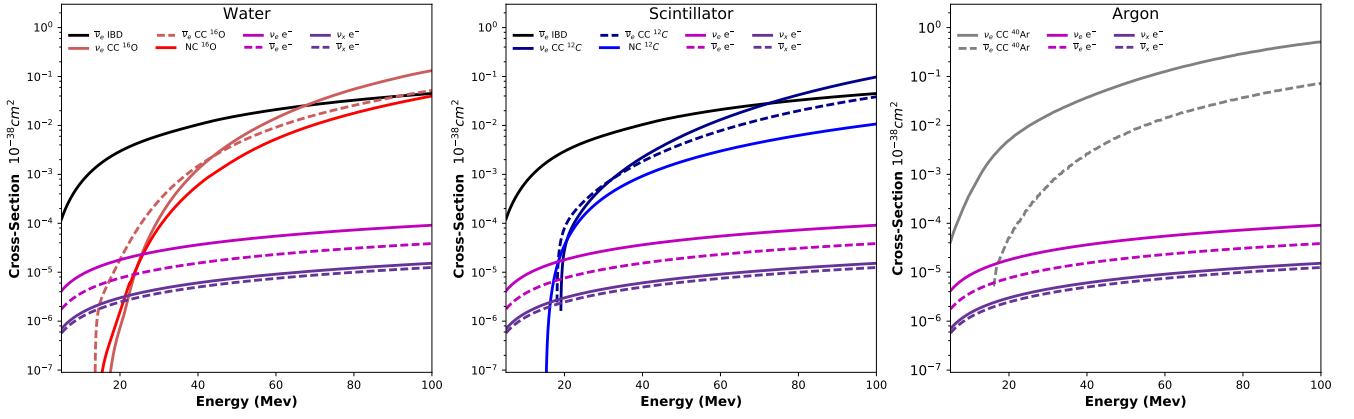


Figure 1. Above are the energy-dependent cross sections for the neutrino-matter interactions in water (left), scintillator (center), and liquid argon (right). These cross sections were provided by the SNOwGLoBES software (Beck et al 2013), and we focus on the neutrino energies up to ~ 100 MeV.

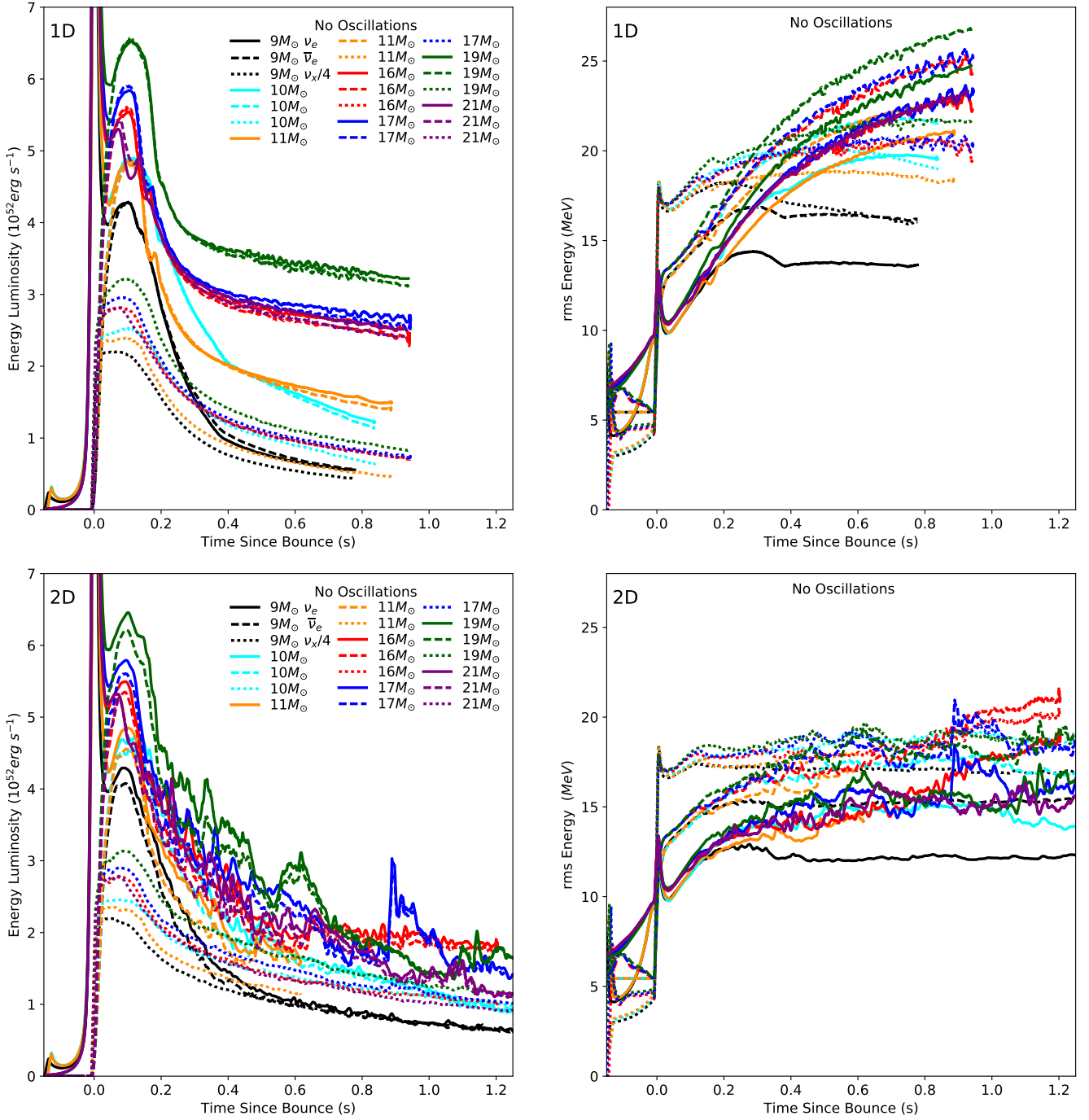


Figure 2. Energy luminosities (in units of $10^{52} \text{ erg s}^{-1}$) and root-mean-square (rms) neutrino energies (in units of MeV) for all the 1D non-exploding models (top two figures) and 2D exploding models (bottom two figures) for the no-oscillation case. The solid curves are for the ν_e s, the dashed curves are for the $\bar{\nu}_e$ s, and the dotted curves are for the “ ν_{μ} s” ($\times \frac{1}{4}$).

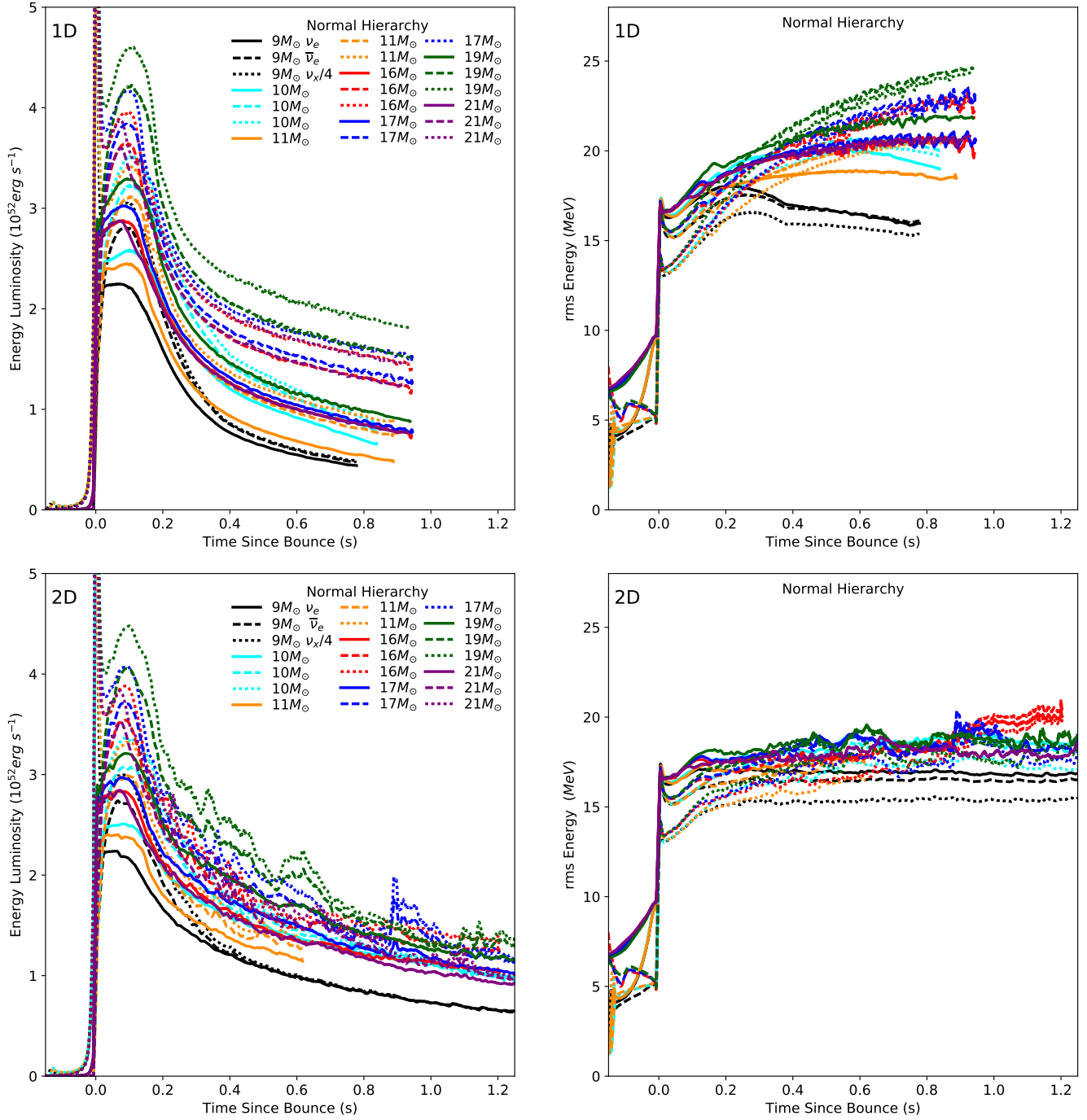


Figure 3. Energy luminosities (in units of $10^{52} \text{ ergs s}^{-1}$) and root-mean-square (rms) neutrino energies (in units of MeV) for all the 1D non-exploding models (top two figures) and 2D exploding models (bottom two figures) for the normal-hierarchy oscillation case. The solid curves are for the ν_e s, the dashed curves are for the $\bar{\nu}_e$ s, and the dotted curves are for the “ ν_{μ} s” ($\times \frac{1}{4}$).

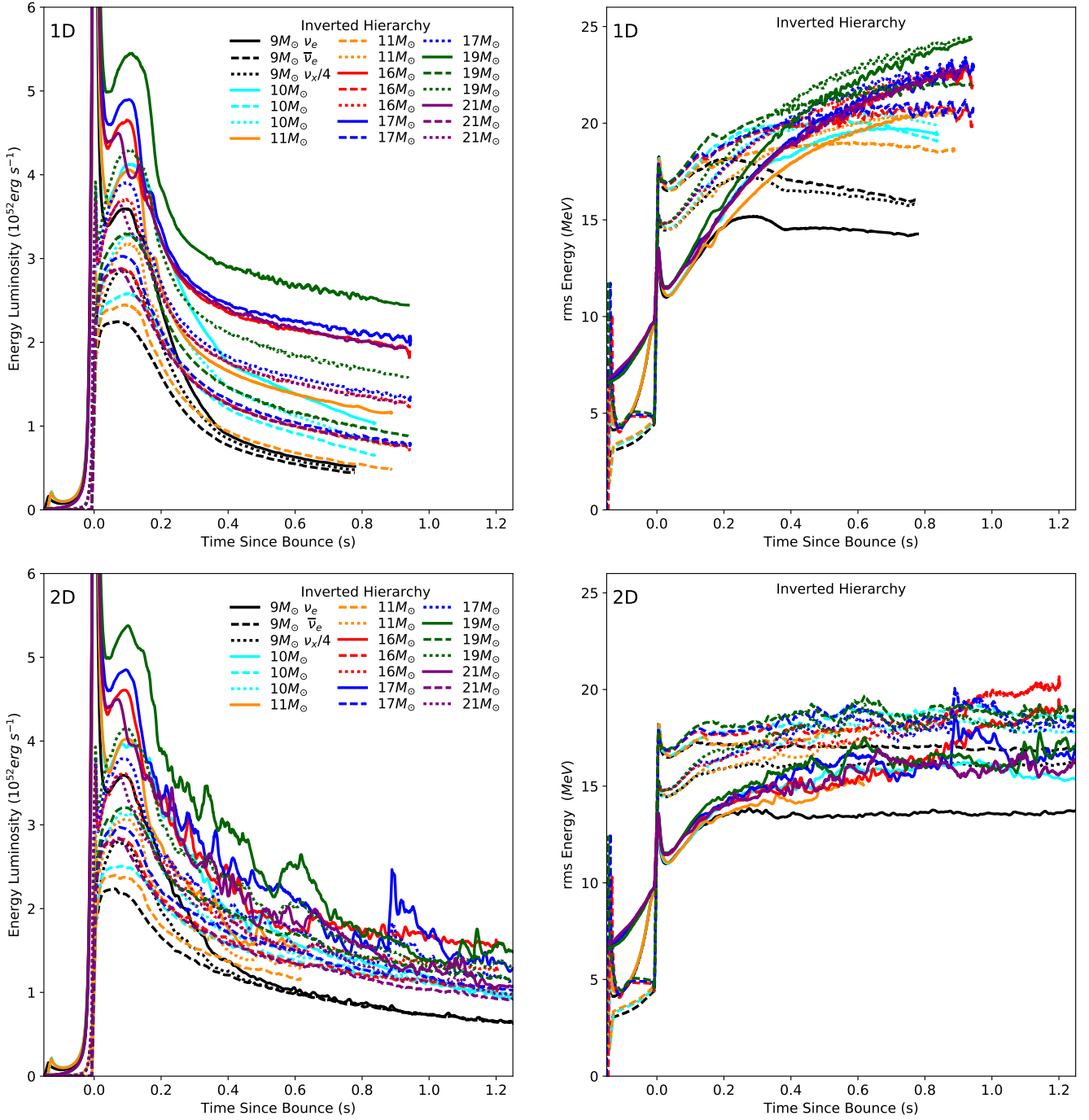


Figure 4. Energy luminosities (in units of $10^{52} \text{ erg s}^{-1}$) and root-mean-square (rms) neutrino energies (in units of MeV) for all the 1D non-exploding models (top two figures) and 2D exploding models (bottom two figures) for the inverted-hierarchy oscillation case. The solid curves are for the ν_e s, the dashed curves are for the $\bar{\nu}_e$ s, and the dotted curves are for the “ ν_{μ} s” ($\times \frac{1}{4}$).

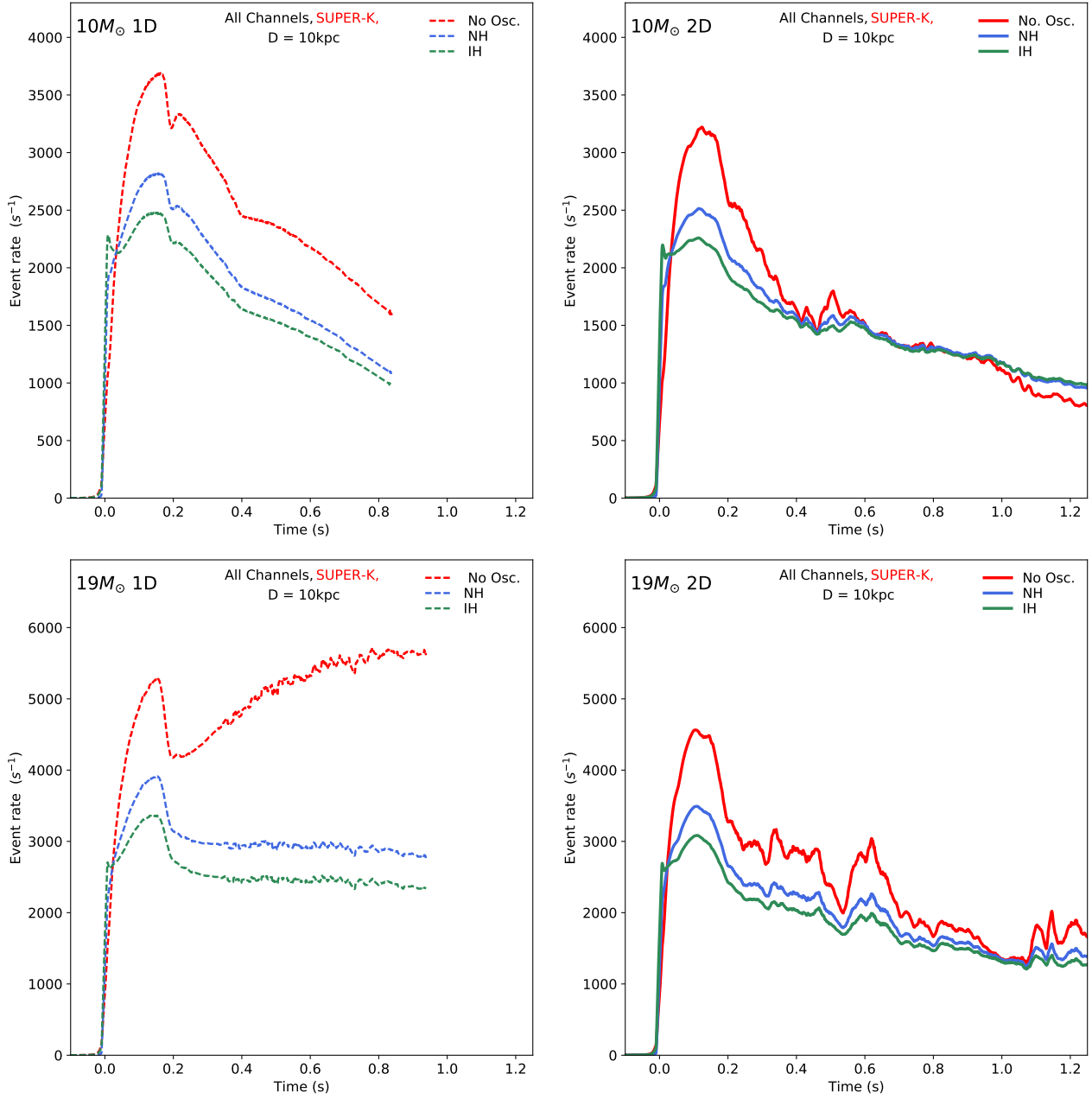


Figure 5. The total, all-channel, event rates (in units of s^{-1}) in **Super-K** at 10 kiloparsecs for all three oscillation models in 1D (left) and 2D (right) for the $10M_{\odot}$ progenitor model (top two plots) and the $19M_{\odot}$ progenitor model (bottom two plots). Note that the 1D models are all here plotted as dashed, while the 2D models are all solid. The no-oscillation case is in red, the normal-hierarchy case is in blue, and the inverted hierarchy case is in green.

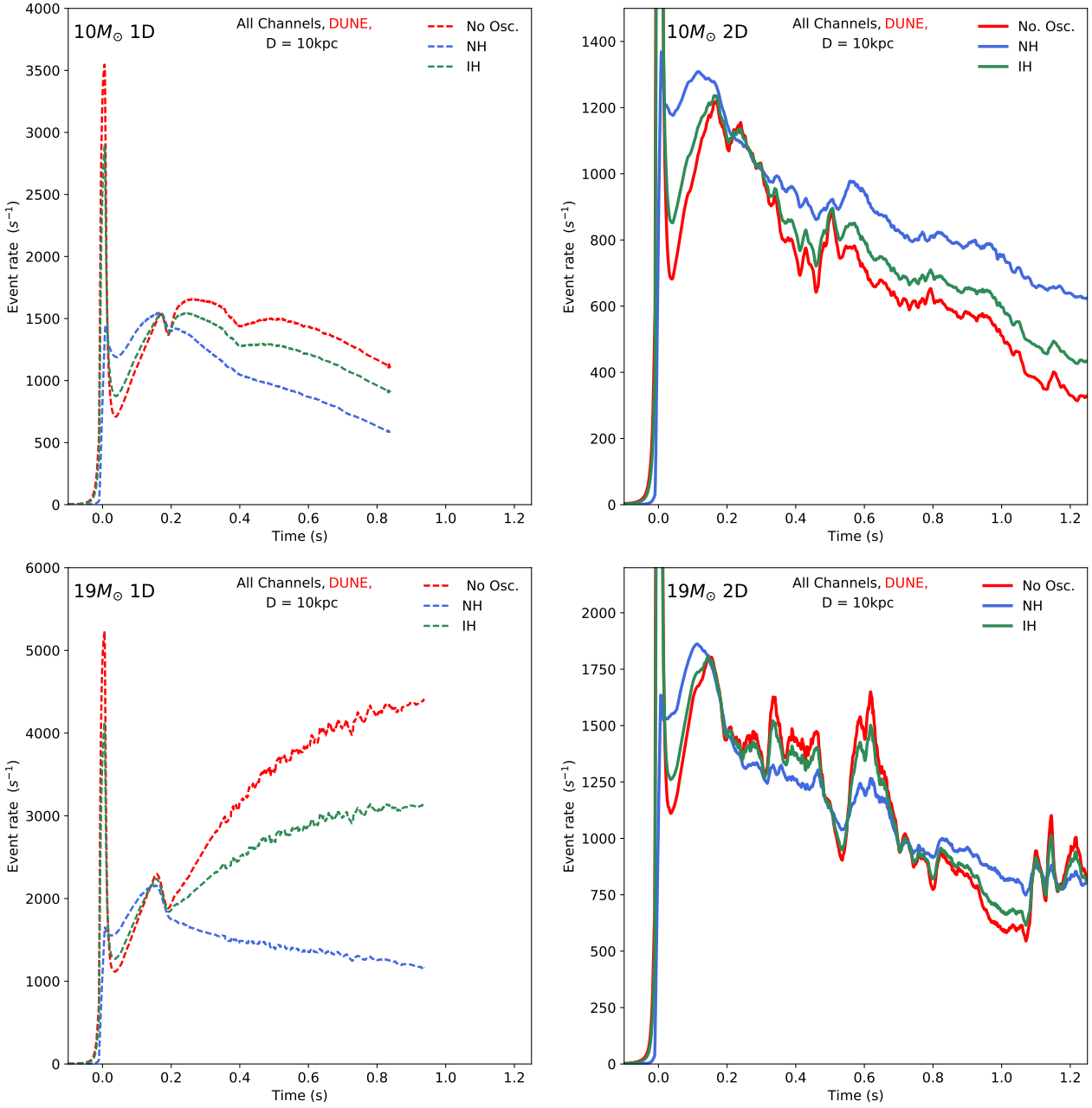


Figure 6. The total, all-channel, event rates (in units of s^{-1}) in **DUNE** at 10 kiloparsecs for all three oscillation models in 1D (left) and 2D (right) for the $10M_{\odot}$ progenitor model (top two plots) and the $19M_{\odot}$ progenitor model (bottom two plots). As in Figure 5, the 1D models are all plotted as dashed, while the 2D models are all solid.

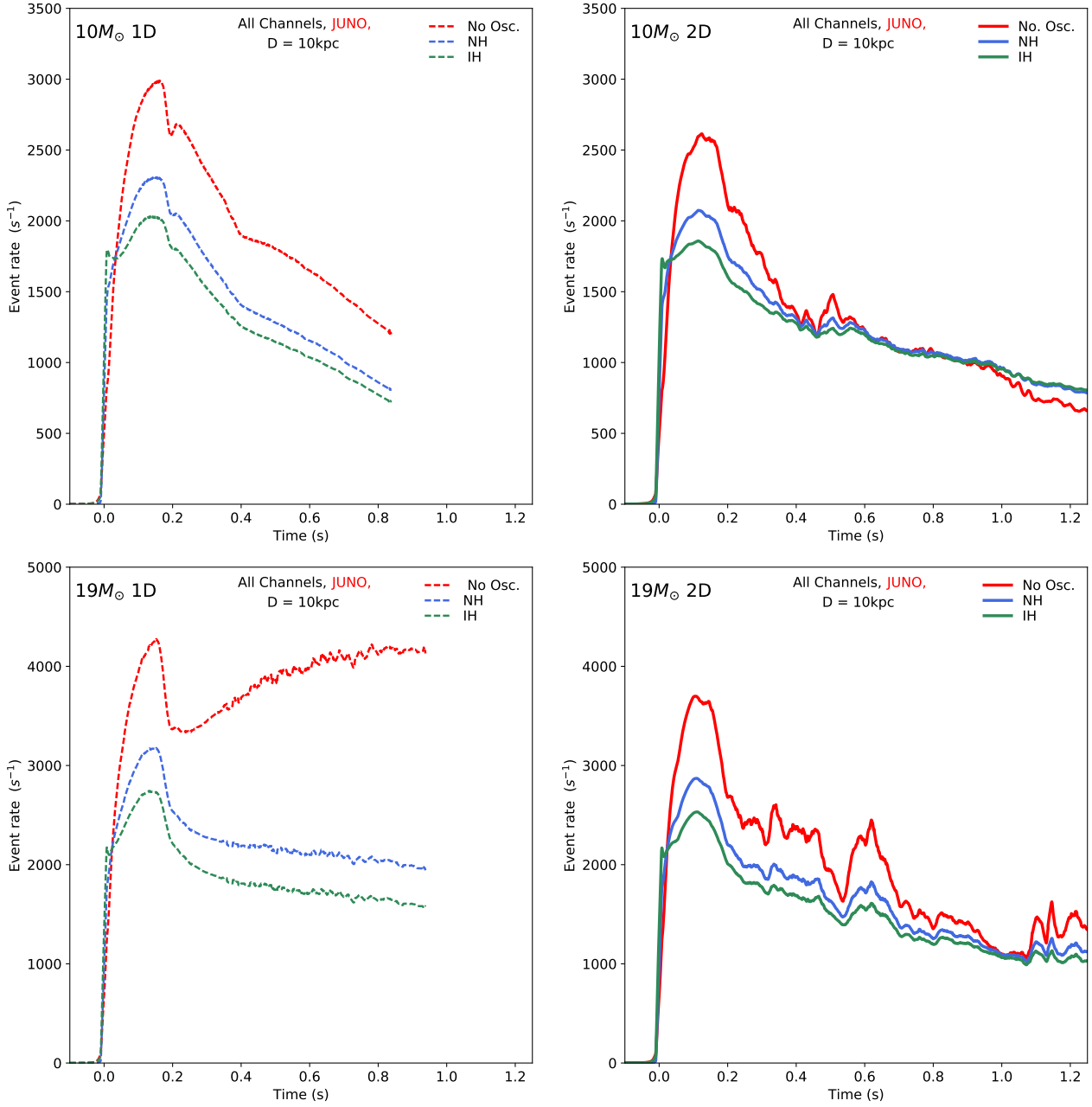


Figure 7. The total, all-channel, event rates (in units of s^{-1}) in JUNO at 10 kiloparsecs for all three oscillation models in 1D (left) and 2D (right) for the 10- M_{\odot} progenitor model (top two plots) and the 19- M_{\odot} progenitor model (bottom two plots). As in Figure 5, the 1D models are all plotted as dashed, while the 2D models are all solid.

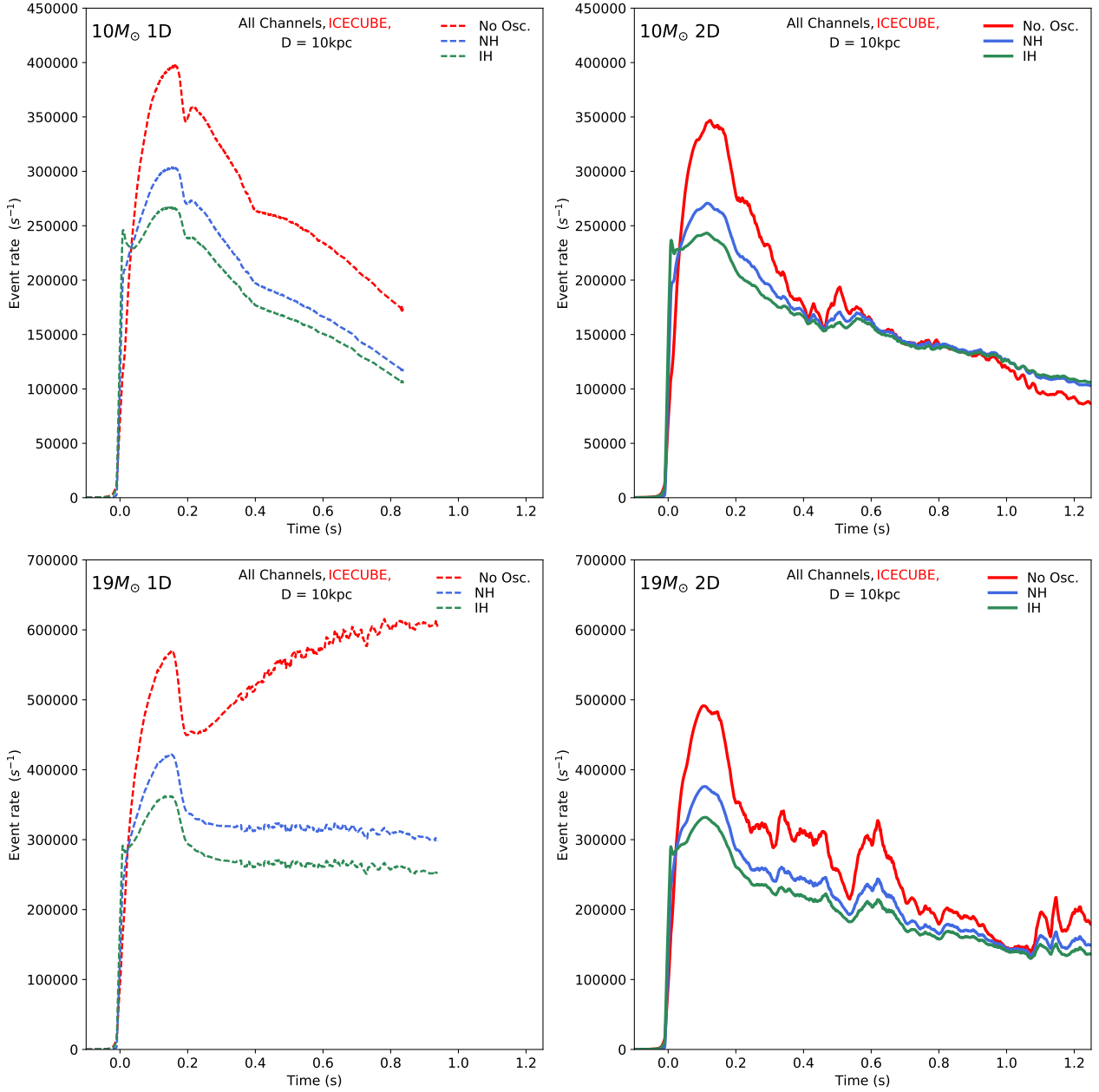


Figure 8. The total, all-channel, event rates (in units of s^{-1}) in IceCube at 10 kiloparsecs for all three oscillation models in 1D (left) and 2D (right) for the $10M_{\odot}$ progenitor model (top two plots) and the $19M_{\odot}$ progenitor model (bottom two plots). As in Figure 5, the 1D models are all plotted as dashed, while the 2D models are all solid.

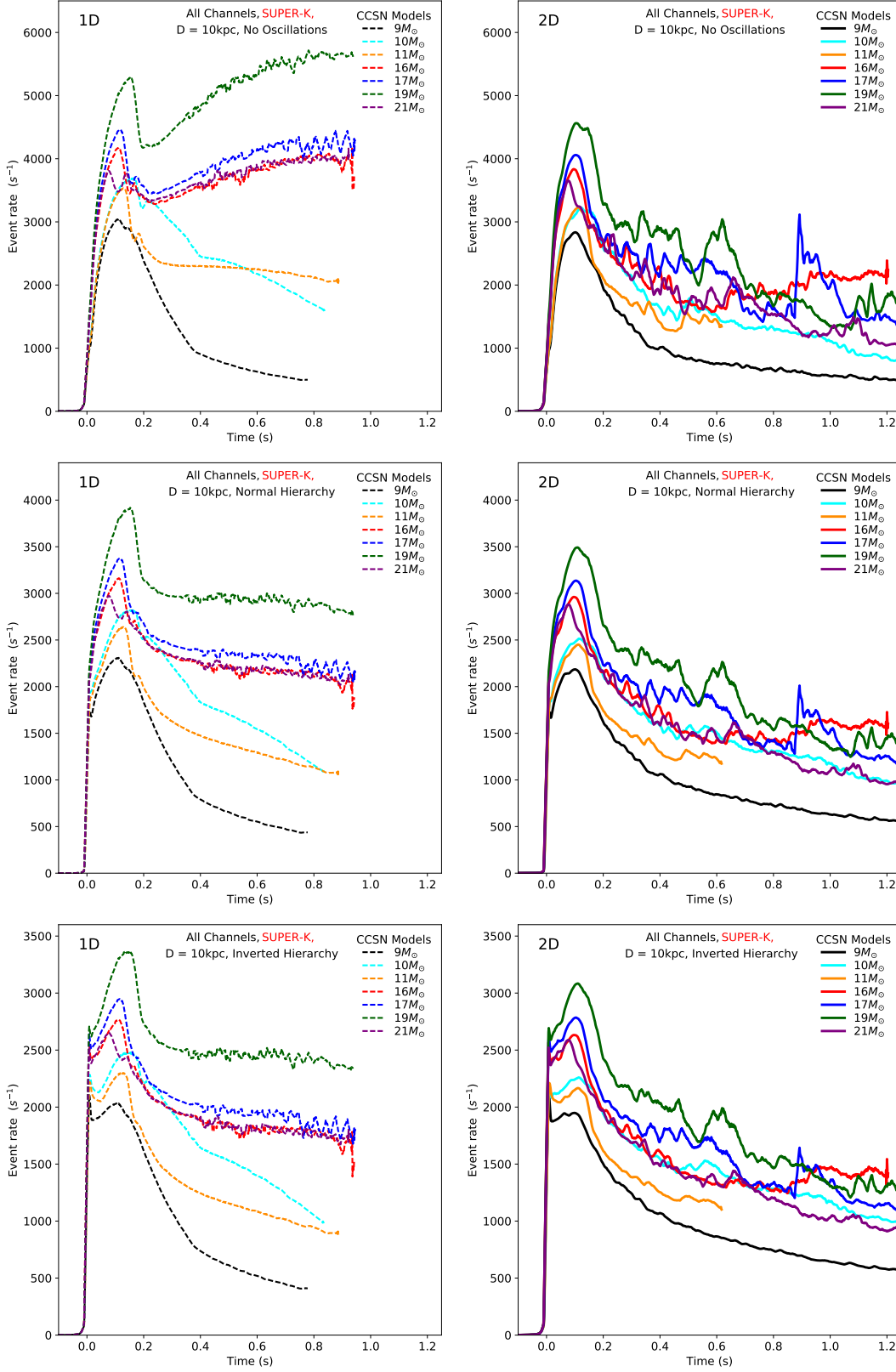


Figure 9. The total, all-channel, event rates (in units of s^{-1}) in **Super-K** at 10 kiloparsecs in the 1D (non-exploding) and 2D (exploding) calculations for all the progenitor models (9 , 10 , 11 , 16 , 17 , 19 , and $21 M_{\odot}$) addressed in this study. The left plots are for the 1D models (in this paper, non-exploding) and the right plots are for the 2D models (exploding). The non-oscillation cases are in the top pair of figures, the normal hierarchy results are depicted in the middle pair, and the inverted hierarchy results are shown in the bottom pair (again, 1D [left], 2D [right]). As above in Figures 5 through 8, the 1D models are all plotted as dashed, while the 2D models are all solid.

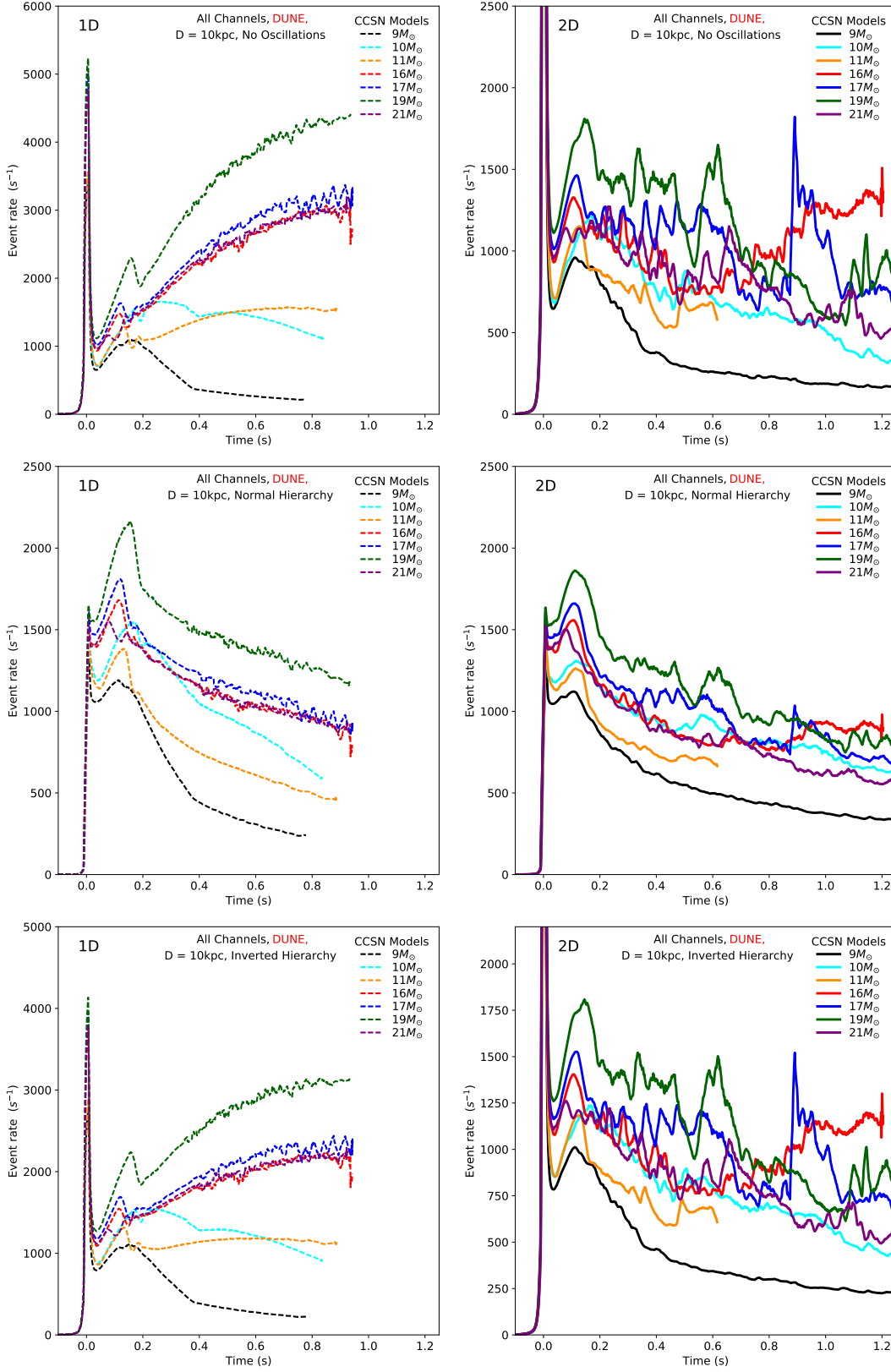


Figure 10. The same as Figure 9, but for DUNE.

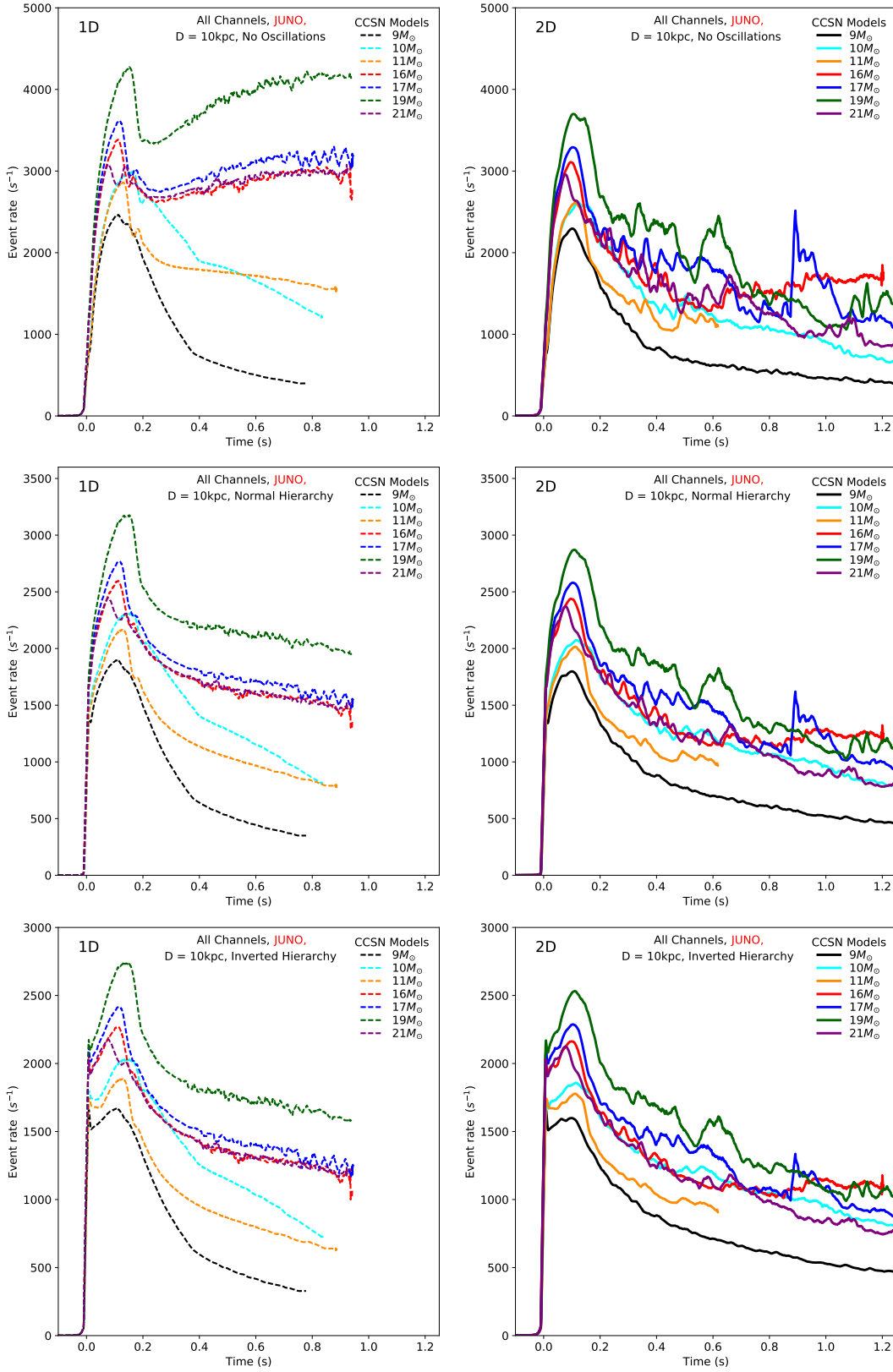


Figure 11. The same as Figure 9, but for JUNO.

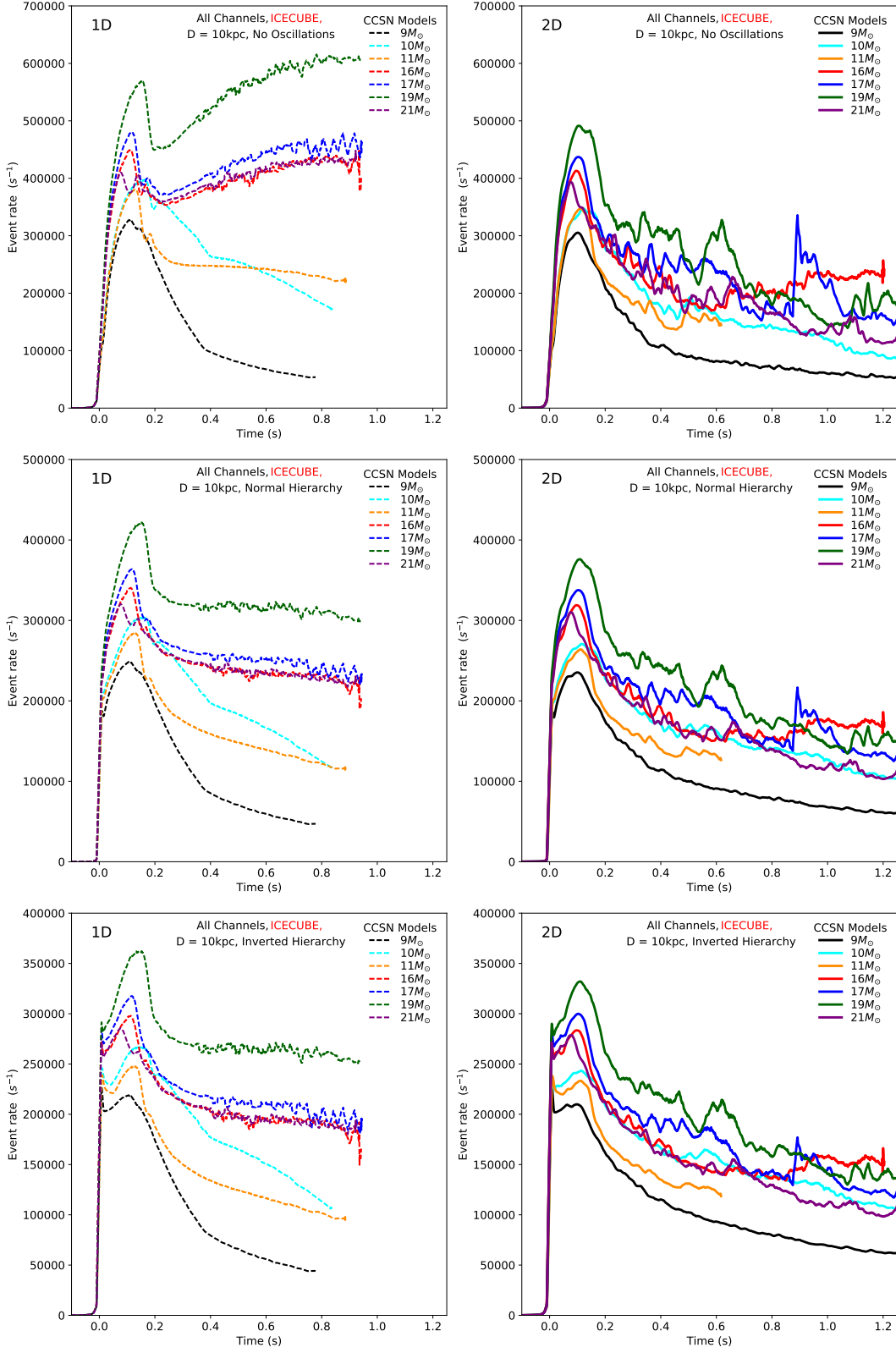


Figure 12. The same as Figure 9, but for IceCube.

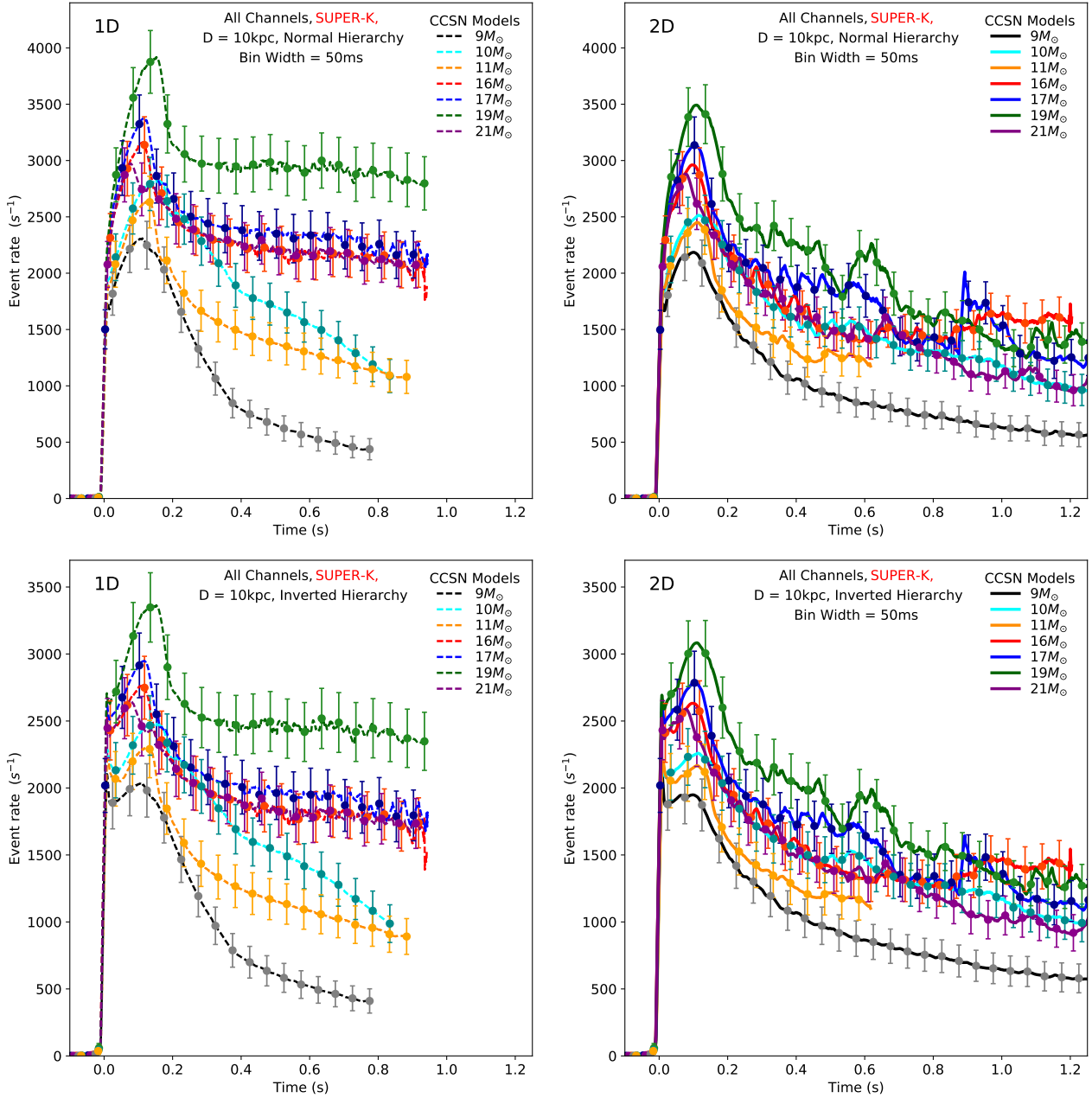


Figure 13. Similar to what is plotted in Fig. 9, this plot reprises the total event rates (in units of s^{-1}) in **Super-K** at 10 kiloparsecs and versus time after bounce, assuming the normal hierarchy (top) and inverted hierarchy (bottom) for all the 1D and 2D progenitor models highlighted in this paper. Also included, however, are error bars in these signal rates assuming 50-millisecond time bins and Poissonian noise. See text for a discussion.

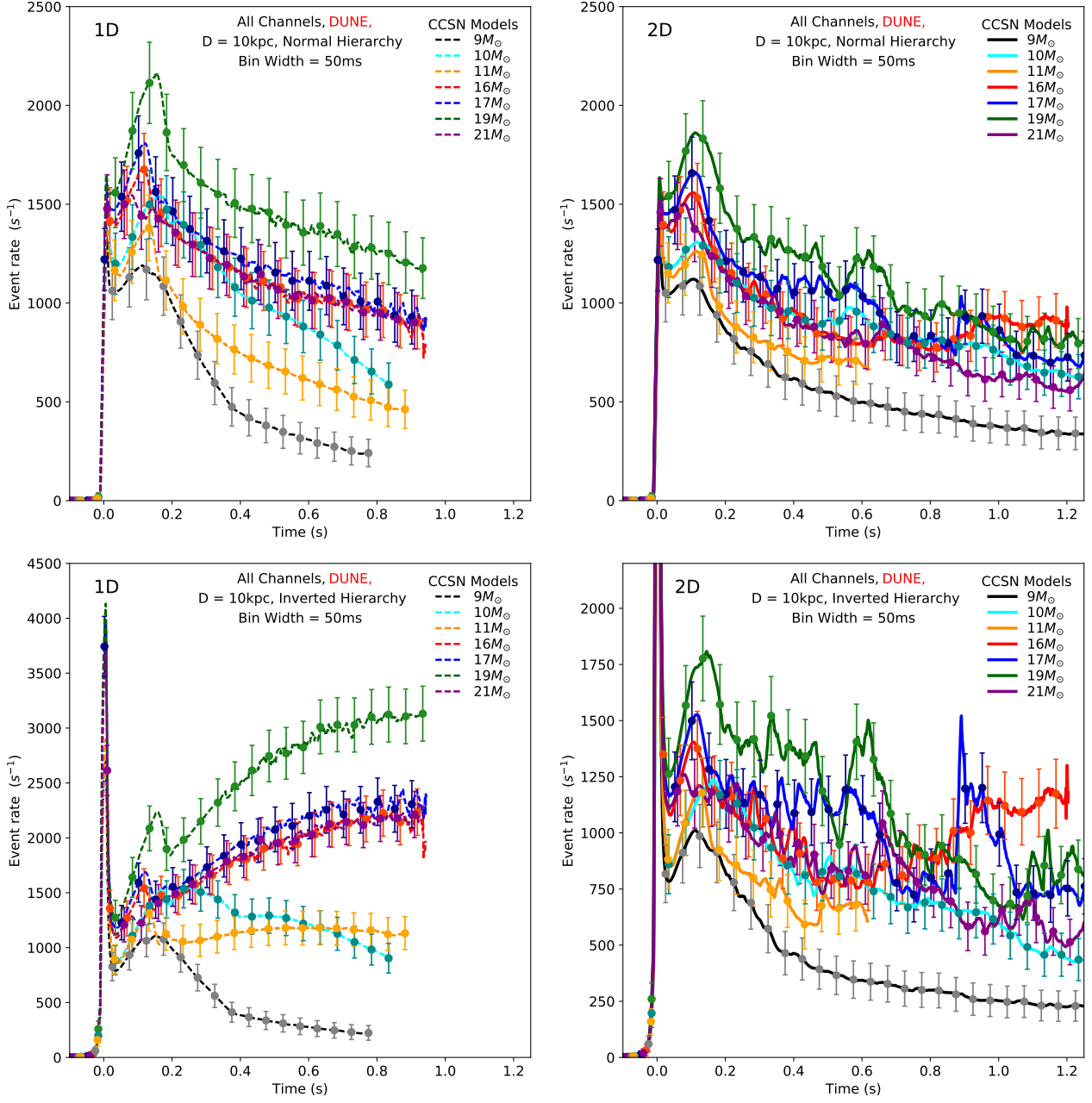


Figure 14. Same as Fig. 13, but for DUNE.

This paper has been typeset from a $\text{\TeX}/\text{\LaTeX}$ file prepared by the author.